Azerbaijan Journal of Physics

FİZİKA

1

www.physics.gov.az

E

XXXI

2025

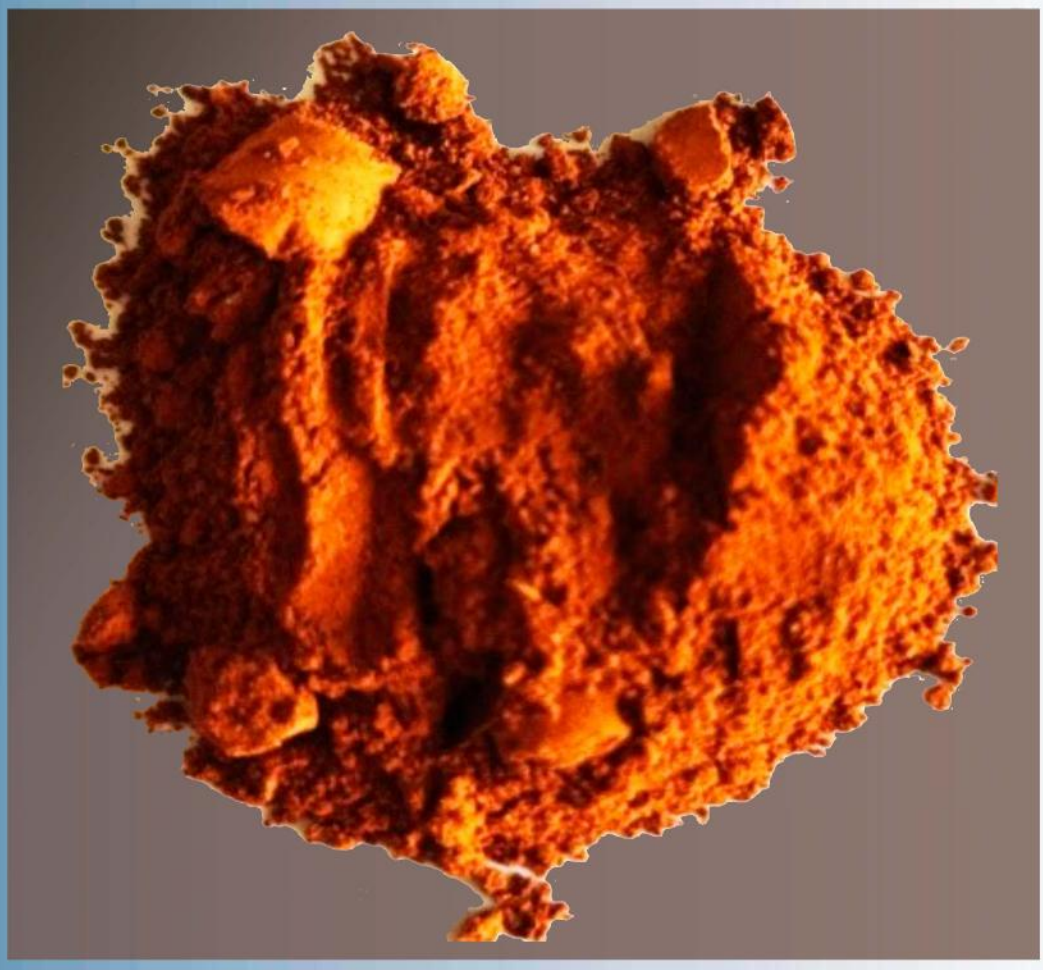

Published from 1995
Ministry of Press and Information
of Azerbaijan Republic,
Registration number 514, 20.02.1995

ISSN 1028-8546
vol. XXXI, Number 01, 2025
Section: E

Azerbaijan Journal of Physics

FIZIKA

Ministry of Science and Education Republic of Azerbaijan
Institute of Physics

PUBLISHING OFFICE

131, H. Javid ave., AZ-1073, Baku
Ministry of Science and Education Republic of Azerbaijan
Institute of Physics

Tel.: (99412) 539-51-63, 539-32-23
Fax: (99412) 537-22-92
E-mail: jophphysics@gmail.com
Internet: www.physics.gov.az

It is authorized for printing:

PHOTOCONDUCTIVITY OF $(GaSe)_{0.8}(InSe)_{0.2}$ MONOCRYSTAL AND INFLUENCE ON IT OF IRRADIATION WITH γ-QUANTUMS

A.Z. ABASOVA, L.H. HASANOVA, A.Z. MAHAMMADOV, S.A. JAHANGIROVA
Baku State University, Baku, Azerbaijan, AZ1148, 23 Z. Khalilov st.
e-mail: vagif_salmanov@yahoo.com

The spectral characteristics of photoconductivity with ordinary and polarized light at different temperatures in $(GaSe)_{0.8}(InSe)_{0.2}$ crystals were analyzed, and it was shown that their nature corresponds to that of GaSe. The effect of γ-ray irradiation was not observed.

Keywords. Solid solution, laser, exciton annihilation, carrier recombination, spectral characteristics.
DOI:10.70784/azip.1.2025103

For a long time, the production of semiconductor compounds belonging to the $A^{III}B^{V}$ group and their solid solutions has been a focus of research. The chemical nature and structural characteristics of $A^{III}B^{V}$ type compounds are of particular interest when studying their photoelectric properties. Their layered monocrystals resemble $A^{II}B^{VI}$ compounds (such as CdS and CdSe) in terms of atomic coordination and the nature of the bonding, which gives them very high photoconductivity [1].

Like other layered crystals from the $A^{III}B^{V}$ group, GaSe and InSe monocrystals also have a defective structure, and the role of defects with a high concentration is significant in the formation of photoconductivity. The defects can be controlled by introducing various amounts of different dopants into the crystals and irradiating them.

Due to their favorable parameters for applications in optoelectronics, microelectronics, and solar energy utilization, GaSe and InSe compounds are more widely studied.

In the present study, some photoelectric properties of $(GaSe)_{0.8}(InSe)_{0.2}$ solid solution monocrystals, which exhibit high photosensitivity over a wide optical range, were investigated, along with the effect of γ-ray irradiation on them.

The Ga-In-Se ternary system is characterized by limited crystal formation up to 10 mol % GaSe or 20 % InSe, or the formation of the unstable ternary compound Ga_2InSe_3. Crystals with the composition $(GaSe)_{0.8}(InSe)_{0.2}$ differ significantly from the initial components, which is why this specific composition was studied. The samples under investigation were synthesized by taking stoichiometric amounts of the GaSe and InSe compound ligatures, and their monocrystals were grown using the Bridgman and Czochralski methods.

Based on their physical properties, the obtained pure crystals can be divided into two groups (Group I and Group II). The specific resistance of Group I crystals was $\rho = 10^2 - 10^4$ Ω·cm, while the high-resistance Group II crystals had a resistance of $\rho = 10^8 - 10^9$ Ω·cm. Silver paste was applied to the 5×3×0.8 mm³ samples to form ohmic contacts. The investigation of the voltage-current characteristic revealed that, at applied voltages up to 100 V, the voltage-current characteristic was linear for Group I crystals, while for Group II crystals, it was exponential. This dependence can be explained by the volumetric inhomogeneity present in the studied crystals.

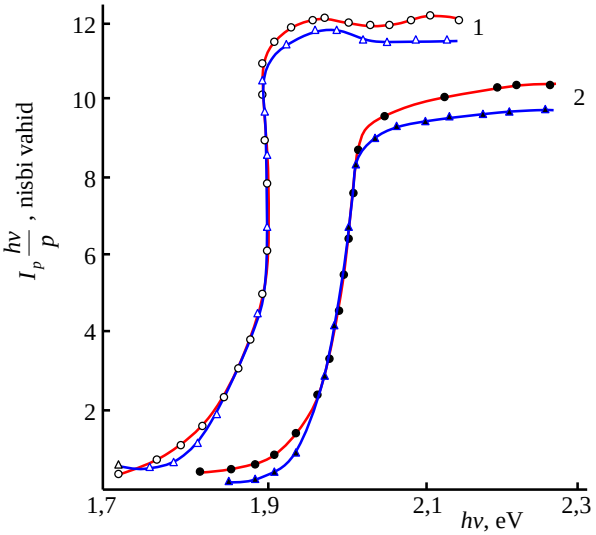

Fig. 1. Photoconductivity curves of Group I $(GaSe)_{0.8}(InSe)_{0.2}$ crystals at 300 K (1) and 77 K (2) temperatures, measured with polarized light (in blue) and ordinary light (in red).

131, H.Javid ave, AZ-1073, Baku
Institute of Physics
E-mail: jophphysics@gmail.com

The photoconductivity of $(GaSe)_{0.8}(InSe)_{0.2}$ crystals was measured at 77 K and 300 K using both ordinary and polarized light. The light was applied perpendicular to the layers, while the electric field was applied parallel to the layers. The light was modulated at a frequency of 30 Hz. The spectral dependence of the photoconductivity for Group I crystals is shown in Figure 1. In all the samples tested, a maximum was observed at an energy of 1.9 eV at room temperature and 2.0 eV at 77 K. These maxima can be explained by the annihilation of excitons. For Group I samples, the decrease in photoconductivity was found to be consistent with the calculated value for the width of the forbidden zone, which corresponds to the forbidden zone width of GaSe crystals [2, 3, 4].

Therefore, the similarity of the properties of GaSe was observed in $(GaSe)_{0.8}(InSe)_{0.2}$ crystals. However, unlike in [1], no effect of light polarization on photoconductivity was observed.

In Group II crystals, no maximum was observed at room temperature, which could be explained by exciton annihilation (Figure 2).

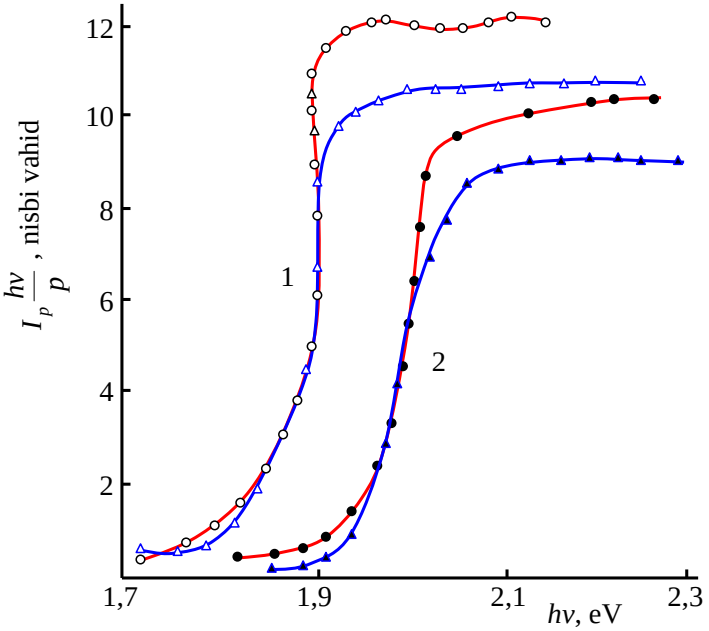

Fig. 2. Photoconductivity curves of Group II $(GaSe)_{0.8}(InSe)_{0.2}$ crystals at 300 K (1) and 77 K (2) temperatures, measured with polarized light (in blue) and ordinary light (in red).

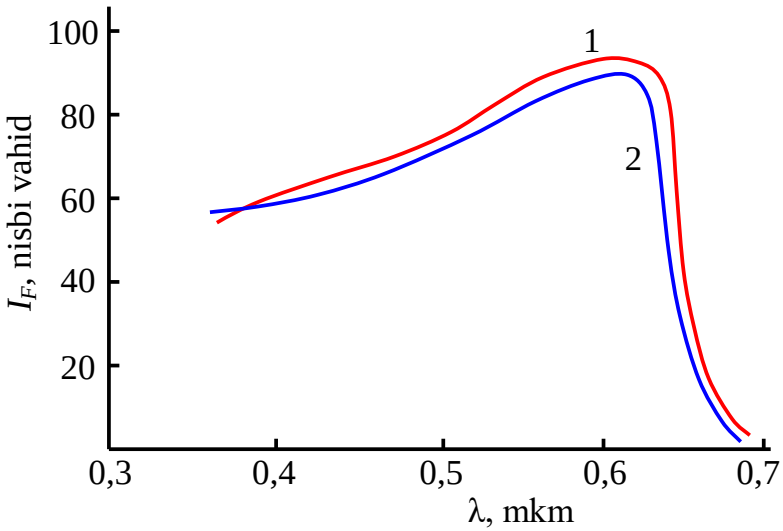

Fig. 3. Spectral dependence of photoconductivity for Group I $(GaSe)_{0.8}(InSe)_{0.2}$ crystals at 300 K, measured with ordinary light: 1 – before irradiation; 2 – after γ-ray irradiation.

However, when the temperature was reduced to 77 K, a negative photoconductivity region appeared in the spectral dependence of the photoconductivity. Such a characteristic is also observed in many photosensitive materials [2–4]. Since the studied compound is GaSe-type and GaSe exhibits p-type conductivity, the negative photoconductivity can be explained by the role of levels with small capture cross-sections near the top of the valence band, which are involved in conductivity. When the crystal is illuminated with low-energy photons from the forbidden zone, electrons in these levels are excited

into the conduction band. However, they are quickly captured by recombination centers and subsequently recombine with free holes, resulting in a decrease in the concentration of free charge carriers and the observation of negative photoconductivity. From the spectral dependence of photoconductivity, the width of the forbidden zone for these types of samples was calculated to be 1.85 eV.

As seen in the figure, as the temperature decreases, the long-wavelength edge of the photoconductivity shifts toward shorter wavelengths. Based on this shift, the temperature coefficient of the forbidden zone width was calculated to be 6×10^{-4} eV/K for Group I crystals and 4×10^{-4} eV/K for Group II crystals.

The difference observed in the physical properties of various samples of the $(GaSe)_{0.8}(InSe)_{0.2}$ crystal is explained by the presence of inhomogeneity. As a result, peaks in the spectrum, which would normally be attributed to exciton annihilation, are not observed.

The study also investigated the effect of γ-ray irradiation with a dose of 2.58×10^2 Kr/kq on the photoconductivity of Group I $(GaSe)_{0.8}(InSe)_{0.2}$ crystals. It was determined that the crystals are resistant to this level of irradiation (Figure 3).

---

[1] *V.P. Mushinsky, M.I. Karaman.* Photoelectric and luminescent properties of indium and gallium chalcogenides.: Shtiintsa, Chisinau. 1975, 79 p.

[2] *K. Maschke, Ph. Schmid.* Phys. Rev., Influence of stacking disorder on the electronic properties of layered semiconductors, 1975, B12, 4312.

[3] *V.M. Salmanov, A.G. Huseynov, R.M. Mamedov, F.Sh. Akhmedova, A.M. Aliyeva*. Photoluminescence of GaS-GaSe heterostructures under two- and three-photon excitation by laser radiation, Russian Physics Journal, 65(9), 2023, 1475-1481.

[4] *Z.T. Kuznicki, K. Maschke, Ph. Schmid.* Influence of stacking disorder on the photoconductivity of GaSe J. Phys.C, Sol.St. Phys. 1979, 12, 3749.

Received: 26.12.2024

STRUCTURAL COMPLEXITY OF THE MATERIALS AND SUPERCONDUCTIVITY: HOW FUNDAMENTAL IS THE MECHANISM INDUCING THIS PHENOMENON OF NATURE

FIZULI MAMEDOV
Institute for Physical Problems, Baku State University, Azerbaijan
e-mail: mail.quanta02@gmail.com, phone: (994) 12 510 18 22

The structural complexity aspect of the materials reveals itself in the superconductivity of the metals. A complex, multisided behavior of the superconducting materials is analyzed in this work. It is shown that there is a subtle balance between superconductivity property of materials and their latent heat of fusion. This feature of superconducting materials manifests itself sharply especially in the case of the so called conventional superconductors, for the indium, lead, tin and mercury. The Cooper pairs analogue formation possibility of the atomic nuclei of the superconducting metals is also considered This analysis strongly supports the idea that electroweak gauge boson masses are manifestation of the fundamental level structural complexity inherent to our universe.

Keywords: dependence of the structural complexity on the energy, the connection between the charges and masses of the elementary particles, structural complexity - latent heat of fusion connection of the substances, the latent heat of fusion and critical temperature dependence for the metals.
DOI:10.70784/azip.1.2025106

INTRODUCTION

As it was discussed in the previous works ([1], [2])

$$M_W/g = M_B/g' \quad (1)$$

type of connection between the masses and coupling constants of the electroweak gauge bosons leads to the emergence of the W boson and Z boson in a succinct, natural form. Eq. (1) can also be interpreted as a connection between the energy and structural complexity of the system. It was indicated that this kind of relation holds for all the known elementary particles, but only in an approximate form. This equation can also be interpreted as a connection between the energy and the structural complexity of the system, their direct proportionality relation. Energy and structural complexity manifest themselves in the form of the mass and coupling constants in this equation. We can observe a similar behavior in the case of superconductors too, at least in the form of the inverse proportionality of the molecular mass of the particular substance and Bose – Einstein condensate critical temperature for this substance [7]. One can also observe trends between the superconductivity temperature of metals and their main physical properties in the wide range, such as latent heat of fusion, crystal structure and nuclear binding energy per nucleon.

METHODS

A. The connection between masses and the structural complexity of the system

Charm quark has a bigger charge (coupling constant) and bigger mass than strange quark has these parameters. Similar relations hold for the top quark – bottom quark, charged lepton – corresponding neutrino relations. Let's pay attention that here what is important is the particle's charge (coupling constant) after the shift in the symmetry, but not its place isospin wise, heavier leptons have the original isospin number $I_W = -1/2$ and heavier quarks have $I_W = ½$.

Charge conjugation operator aspect of the electron wave function also confirms this interpretation of the equation above. Charge conjugation operator changes a negative - energy solution for the electron with the certain momentum p_i and polarization S_i to a positive - energy solution with the same p_i and S_i:

$$\Psi_C = C\gamma_0\Psi^* = C\gamma_0((\varepsilon\gamma_i p^i + m)/(2m))^*(1 + \gamma^5(p_i S^i)/2)^*\Psi^* \rightarrow (-\varepsilon\gamma_i p^i + m)/(2m)(1 + \gamma^5(p_i S^i)2)\Psi_C \quad (2)$$

Here ε = 1 for positive energy states and ε = -1 for negative energy states.

When applied to Eq.(1), we can say that both numerator and denominator change sign which has no impact on the equation. Only the magnitude of the coupling constant, in this particular case the electric charge, is important for the energy – structural complexity relations. The exact nature of Eq.(1) indicates that the electroweak gauge bosons are indeed the fundamental level of particles, the intermediaries of the fundamental level of interactions.

The Bose – Einstein condensate critical temperature, the temperature playing vital role in superconductivity [8],

$$T_c = 2\pi\hbar^2/mk_B\lambda_c^2 \quad (3)$$

is inversely proportional to the molecular mass of the substance. Here k_B is the Boltzmann constant and λ_c is the thermal wavelength at the critical temperature.

131, H.Javid ave, AZ-1073, Baku
Institute of Physics
E-mail: jophphysics@gmail.com

We can interpret this formula as follows: the bigger the mass the stronger coupling between the molecules of the substance, structural complexity wise, and the breakdown of this complexity occurs at lower temperature. We can treat the superconductivity as a manifestation of the breakdown of the structural complexity of the system also. Eq. (2) is derived for the non interacting gas. Eq. (1) is a key to understanding the W boson, B boson mixing, meanwhile its approximate form is valid when applied to the lepton and quark masses. Similarly, approximate form of Eq. (2) could be valid when applied to metal atoms, latent heat of fusion instead of atomic mass would be more suitable in this case (see next section).

This approach to understanding of the rise of superconducting state is also supported by the isotope mass dependence of this phenomenon. There is a well – known relation [7]

$$T_c = \frac{C}{M^{\frac{1}{2}}} \quad (4)$$

between the isotope mass and temperature of superconductivity of metals. C is constant here.

B. Trends between the physical properties of the superconducting materials and their critical temperature.

In the table below we show the certain physical properties of some metals which are likely to play significant role in the superconductivity of the metals. Most of these metals exhibit superconductivity at temperatures significantly distant from the absolute zero temperature.

Physical properties of the superconducting materials

Metal	Atomic number - Atomic Weight (g/mol)	Crystal Structure	Latent heat of fusion		Temperature of superconductivity, K	Nuclear Binding Energy per Nucleon, MeV
			KJ/mol	J/g		
Aluminum, Al	13 - 27	fc cubic	10.7	396	1.2	8.33
Beryllium, Be	4 - 9.1	hexagonal	12.2	1356	0.026	6.3
Cadmium, Cd	64 - 112	hexagonal	6.3	56	0.5	8.5
Indium, In	49 - 115	bc tetragonal, fc cubic	3.26	28.3	3.41	8.5
Iron, Fe	26 - 55.8	bc cubic, fc cubic	13.8	247	0.0	8.8
Lanthanum, La	57 - 138.9	hexagonal	6.2	44.6	5.0	8.38
Lead, Pb	82 - 207	fc cubic	4.77	23	7.2	7.67
Mercury, Hg	80 - 201	rhombohedral, tetragonal	2.29	11.4	α - 4.15 β – 3.95	7.89
Nickel, Ni	28 - 58.7	fc cubic	17.2	293	0.0	8.73
Niobium, Nb	41 - 92.9	fc cubic	26.4	288	9.3	8.66
Tantalum, Ta	73 - 181	bc cubic	36	199	4.48	8.02
Technetium, Tc	43 - 99	hexagonal	24	244.9	7.77	8.61
Thallium, Tl	81 - 204.4	hexagonal	4.14	20.25	2.39	7.88
Tin, Sn	50 - 118.7	bc tetragonal	7.0	59	3.7	8.5
Titanium, Ti	22 - 48	hexagonal	18.7	390	0.39	8.79
Tungsten, W	74 - 183.8	bc cubic	35	190	0.015	8.0
Vanadium, V	23 - 50.95	bc cubic	22.8	448	5.48	8.74

A quick look at this table tells us that all four conventional superconductors, indium, tin, lead and mercury have the specific latent heat of fusion at the lower end values for the specific latent heat of fusion in J/g. One would say that they have noticeably small value for the latent heat of fusion per nucleon. Their structural complexity gets altered by smaller value of energy: according to Eq. (1) the bond holding the structural complexity is weaker and this complexity breaks down at temperatures significantly distant from the absolute zero temperature. Atoms and molecules are not like flamboyant objects moving chaotically in our world, they are more likely follow the certain pattern in their thermal motion: under extreme conditions the whole structure of this pattern breaks down.

Schematically we can depict the above discussed connection between the latent heat of fusion and superconductivity of metals the following way:

Small value of the latent of fusion → low level of the structural complexity → weaker bond between the atoms of the substance → smaller value of the analogue of the coupling constant in Eq. (1) → smaller value of the analogue of the mass in Eq. (1) or Eq. (2) → superconductivity at the temperature significantly distant from the absolute zero temperature.

It catches one's attention that metals (isotopes) with the sizable critical temperature tend to have an odd number of nucleons, that is their nuclei are fermions and can induce their own specific Cooper pairs analogue. The distance between the atomic nuclei of crystals is three – four orders less than the typical distance between the electrons of the Cooper pairs. Vanadium, the superconducting metal, has high value for the latent heat of fusion, but it also has at the higher

end value for its nuclear binding energy per nucleon. Vanadium is not considered as a conventional superconductor, high value of the nuclear binding energy per nucleon might be another venue for the transition of the metal into the superconducting state [2]. The naturally occurring isotopes of iron, Fe^{57}, and nickel, Ni^{61}, have high value of nuclear binding energy per nucleon and fermionic statistics nuclei. These isotopes might also exhibit superconductivity under certain conditions. Iron and nickel have relatively simple crystal structures, face centered cubic and body centered cubic crystal structures. Chances are slim that these isotopes have their own, noticeably low value latent heat of fusion, because the melting point of these metals is not in the region of temperature we usually call extreme conditions (He^3 isotope of helium has significantly smaller values for both the specific heat of vaporization and latent heat of fusion than He^4 isotope has). Nevertheless, if these isotopes exhibit superconductivity, it would be another confirmation of the structural complexity – superconductivity connection scheme. This would also imply that the substances exhibit the structural complexity in different forms. The high value of the nuclear binding energy per nucleon for nickel Ni^{62} could also be another clue to determining the complexity level inherent to our universe.

DISCUSSION AND CONCLUSIONS

The connection between the energy and structural complexity of the quantum mechanical systems reveal itself distinctly in many physical systems, such as the connection of the electroweak interactions coupling constants and electroweak boson masses, latent heat of fusion related properties of the crystals. Superconductivity of metals, this tantalizing phenomenon is analyzed in the frame of the structural complexity of the substances. It is shown that like electroweak gauge boson masses, this phenomenon is the manifestation of the most fundamental feature of nature, its structural complexity. The latent heat of fusion of metals – superconducting temperature connection emerges as a result of this analysis. It is emphasized that not just conducting electrons but also the atomic nuclei of the superconducting metals may generate they own Cooper pairs analogue, since they often tend to be fermions.

ACKNOWLEDGEMENTS

The author would like to thank Sadiyar Rahimov, director of the Institute for the Physical Problems, Baku State University, for the several helpful discussions of the superconducting properties of metals and the phase transitions in crystals.

[1] *F.A. Mamedov*. $SU(2)_L$ x $SU(2)_R$ symmetry of the fermions and the vector bosons, the fermionic origin of the local gauge transformations, the visible traces of the flickering nature of the early stages of the universe's formation, AJP Fizika C, 2023

[2] *F.A. Mamedov.* The connection between the energy and structural complexity of the matter, structural complexity origin of the electroweak boson masses as well as metabolism in living organisms, AJP Fizika C, 2024

[3] *R.W. Brown, K.L. Kowalski, and S.J. Brodsky.* Classical radiation zeros in gauge theory amplitudes, Phys. Rev. D, 28:624, 1983.

[4] *S.L. Glashow*. Partial Symmetries of Weak Interactions, *Nuclear Physics* 22, (1961), 579

[5] *S. Weinberg*, A Model of Leptons, Physical Review Letters, 19, 1264

[6] *A. Salam, N. Svartholm.* Proceedings of the Eighth Nobel Symposium, *Almqvist & Wiksell, Stockholm (1968)*

[7] The Isotope Effect in Superconductivity. I. Mercury *https://doi.org/10.1103/PhysRev.84.691*

[8] Leggett, Anthony J. (2022), Quantum liquids: Bose condensation and Cooper pairing in condensed-matter systems, Oxford: Oxford University Press. ISBN 9780192856944

[9] Binding energy per nucleon, *http://barwinski.net/isotopes*

[10] *Krassimira Marinova, Istvan Angeli*, Nuclear Charge Radii, International Atomic Agency, https://www-nds.iaea.org/radii

[11] Table of Isotopic Masses and Natural Abundances,https://www.chem.ualberta.ca/~masspec/atomic_mass_abund.pdf

[12] National Superconducting Cyclotron Laboratory, Laser precision studies of the nuclear radii. http://nscl.msu.edu/news/news - 25.html
Size of helium nucleus measured more precisely than ever before.

[13] https://www.admin.ch/gov/en/start/documentation/media-releases.msg-id-82143.html

[14] *J.E. Hirsch.* BCS theory of superconductivity: it is time to question its validity, Phys. Scr. 80 (2009) 035702

Received: 28.12.2024

PHOTOLUMINESCENT PROPERTIES OF $CuInS_2$

I.A. MAMEDOVA[a]*, I.Q. QASIMOQLU[a], N.A. ABDULLAYEV[a,b]
[a]Institute of Physics, Ministry of Science and Education of Republic of Azerbaijan, Baku, AZ1073 Azerbaijan
[b]Baku State University, Baku, AZ1148 Azerbaijan
**e-mail: irada_mamedova@yahoo.com*

$CuInS_2$ crystals were grown by the Bridgman method and characterized by X-ray diffraction and Raman scattering methods. Photoluminescence of $CuInS_2$ was studied by confocal laser microscopy. A nonlinear dependence of the luminescence intensity on the intensity of the exciting light was established.

Keywords: $CuInS_2$, exciton, photoluminescence, Raman scattering, confocal laser microscopy
DOI:10.70784/azip.1.2025109

1. INTRODUCTION

Ternary semiconductor compounds $A^I B^{III} C_2^{VI}$ crystallizing in tetragonal chalcopyrite structure have attracted considerable attention due to their potential application in photovoltaic solar energy conversion [1-6]. Ternary semiconductor $CuInS_2$ is considered as one of the most promising materials for the fabrication of thin-film solar cells due to its optimal band gap of 1.5 eV. Solar cell technologies using chalcopyrites $A^I B^{III} C_2^{VI}$ have made rapid progress in recent years [7]. The efficiency of thin-film solar cells based on $CuInS_2$ is ~24%. In [8, 9], the optical absorption of $CuInS_2$ and the band gap at 2°K are 1.55 eV for $CuInS_2$ [8], and in [9] at 300 K the band gap is 1.48 eV. According to [10, 11], the band gap in $CuInS_2$ is 1.3 eV. The luminescent properties were studied in [12-19]. In [12] the luminescence was measured as a function of temperature from 8 to 300 K. Ten different peaks were present in the band edge region. Four peaks at 1.5347, 1.5324, 1.5288, and 1.5281 eV, due to acceptor or donor-bound excitons, were observed at 8 K. It was found that luminescence persisted even at room temperature. These peaks were also observed in [13]. In [17], time-resolved PL spectra of free excitons were obtained and analyzed for the first time for $CuInS_2$ single crystals, and the radiative lifetime of free excitons was obtained at low temperatures. The radiative lifetime of a free exciton A was found to be 320 ± 30 ps at 10 K. $CuInS_2$ quantum dots are promising light emitters, demonstrating a high photoluminescence quantum efficiency (PLQE) of 65% at a long emission wavelength of 920 nm [18].

This paper presents the results of the photoluminescence investigation of $CuInS_2$ at 300 K using confocal laser microscopy, with the aim of obtaining additional information on the photoluminescent properties of $CuInS_2$.

2. EXPERIMENTAL PROCEDURE

The $CuInS_2$ compound was synthesized by direct alloying of the initial ultra-pure components Cu, In and S, taken in a stoichiometric ratio, in quartz ampoules evacuated to 10^{-4} Torr. $CuInS_2$ crystals were grown by the Bridgman method by slow cooling of melts of stoichiometric composition. The obtained crystals were characterized by X-ray diffraction (Fig. 1) and Raman scattering (Fig. 2). $CuInS_2$ crystallizes in a tetragonal structure (space group $I\bar{4}2d$). The lattice parameters are a = 5.519 Å, c = 11.133 Å, c/a = 2.017.

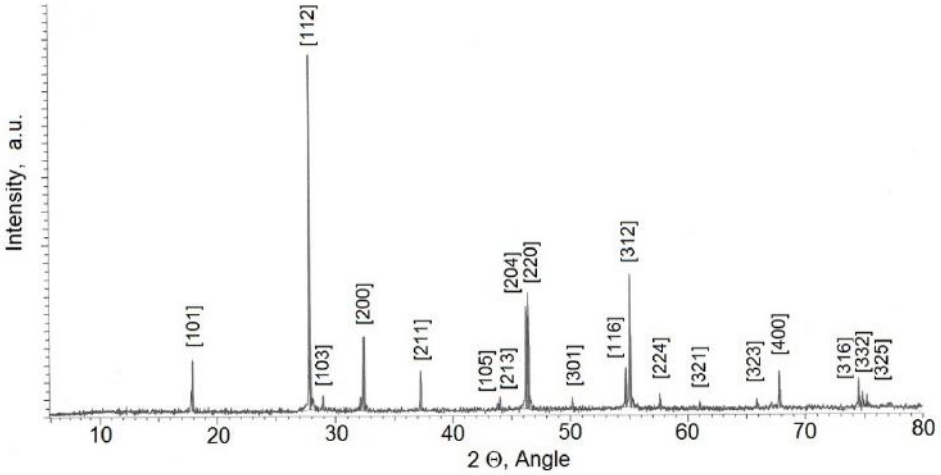

Fig. 1. X-ray diffraction pattern of the compound $CuInS_2$

131, H.Javid ave, AZ-1073, Baku
Institute of Physics
E-mail: jophphysics@gmail.com

The luminescence and Raman scattering spectra of $CuInS_2$ were measured on a Nanofinder 30 confocal Raman microspectrometer (Tokyo Instr., Japan). An Nd:YAG laser with an output wavelength of 532 nm and a maximum power of 10 mW was used as an excitation source. The spectral resolution was no worse than 0.5 cm^{-1}. The radiation detector was a cooled (thermoelectrically to -100^{0}C) CCD camera (1024 by 128 pixels) operating in the photon counting mode. The Raman scattering spectra of $CuInS_2$ were measured in the backscattering geometry in unpolarized light.

3. RESULTS AND DISCUSSION

Fig. 2 shows the Raman spectrum of $CuInS_2$. The spectrum consists of several lines with maxima at 127 cm^{-1}, 257 cm^{-1}, 296 cm^{-1} and 339 cm^{-1}. There are 8 atoms in the primitive cell of CuInS2 crystals, and the vibrational spectrum consists of 24 normal modes, of which 21 are optical, described by the following irreducible representations: Γ=1A_1 +2A_2 + 3B_1 + 3B_2 + 6E, where A_1, B_1, B_2 and E modes are Raman active, B_2 and E modes are also IR active, and A_2 modes are optically inactive [20]. Figure 2 clearly shows the A_1 mode at 296 cm^{-1}.

Fig. 3 shows the photoluminescence spectra of $CuInS_2$ at 300 K at different intensities (1 mW-10 mW) of the exciting light. The spectrum consists of a narrow band with a maximum position at ~811 nm (1.529 eV) and a half-width of 30 nm (55 meV). The position of the maximum does not change with increasing of excitation intensity and is close to the value of the band gap, so this gives reason to believe that this is edge luminescence. The position of the maximum corresponds to the literature data.

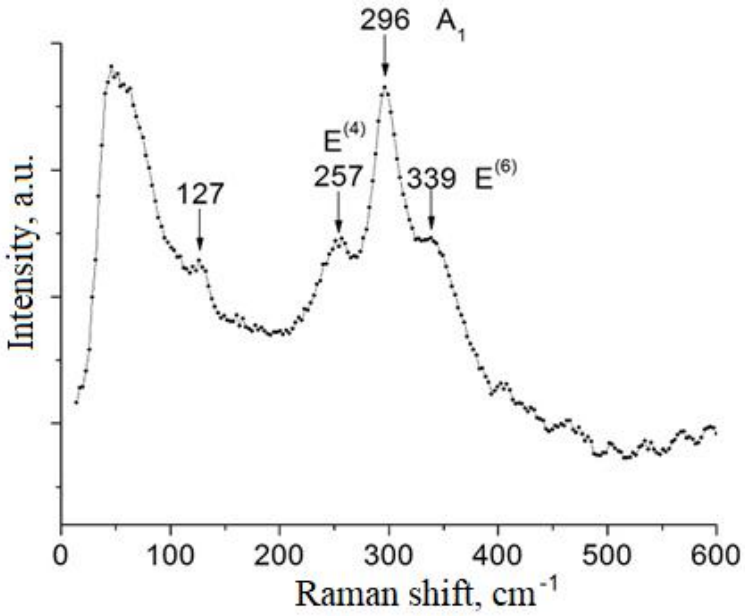

Fig. 2. Raman scattering spectrum of $CuInS_2$ crystals.

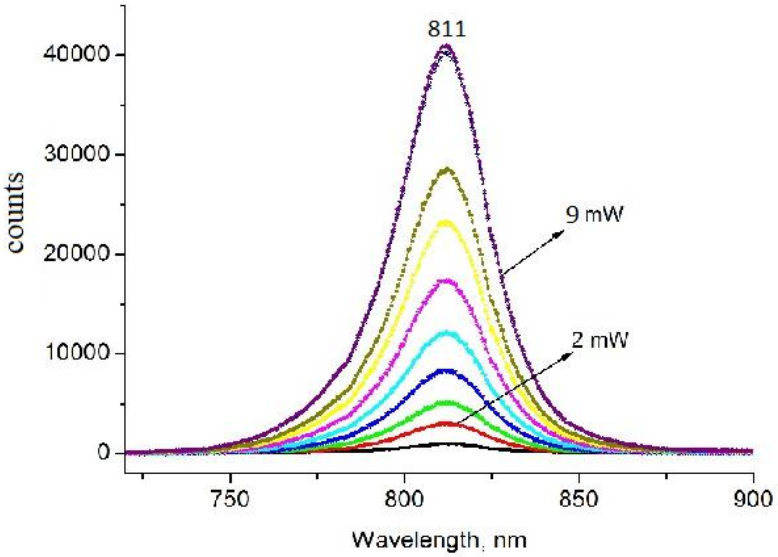

Fig.3. Photoluminescence spectra of $CuInS_2$ at different laser light intensities.

In [8], from studies of the optical absorption edge, the band gap of $CuInS_2$ has a value of 1.55 eV at 2 K, and in [9], at 300 K, the band gap is 1.48 eV. In [14], the PL spectra of pure $CuInS_2$ and doped Yb:$CuInS_2$ were studied. For both crystals, a small PL peak is observed at about 1.50–1.53 eV. The position of the peak almost coincides with the energy of the band gap of $CuInS_2$ ~1.53 eV, and the authors attribute it to exciton recombination. In [21], in high-quality $CuInS_2$ single crystals, sharp exciton peaks were observed in the near-boundary region of the PL spectra at 4.2 K. According to the authors, the lines at 1.536 and 1.554 eV in the spectra are associated with transitions of free excitons. In the PL spectra, the exciton line splits into two peaks at 1.5348 and 1.5361 eV, which the authors attributed to the lower and upper branches of the exciton polariton, respectively.

The exciton nature of photoluminescence is confirmed by the quadratic dependence of the PL intensity on the excitation intensity (Fig. 4).

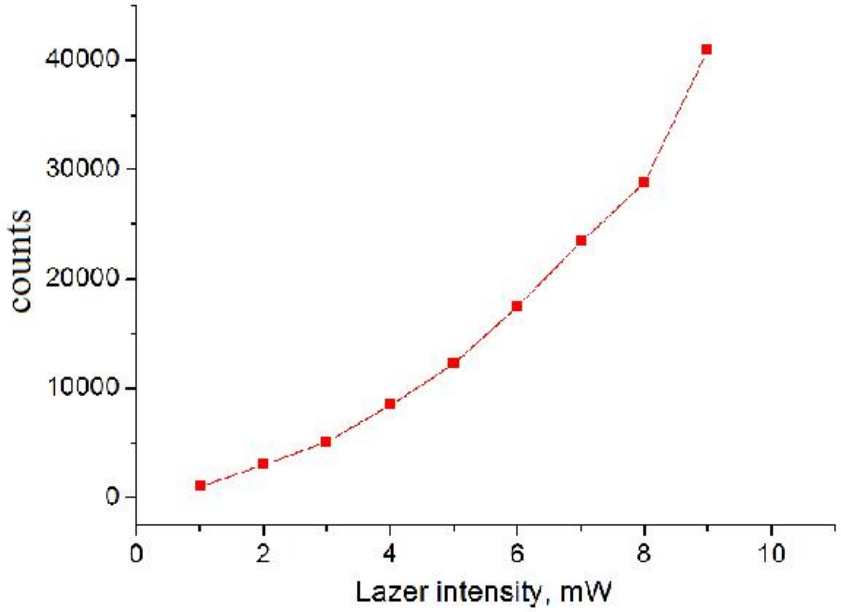

Fig.4. Photoluminescence intensity of $CuInS_2$ as a function of excitation level

Fig.4 shows the dependence of photoluminescence intensity on the intensity of the exciting light. As can be seen, the dependence is nonlinear. Since at the beginning of the dependence, the PL band intensity increases with the excitation level according to the law $I_{PL} \sim I_{ex}^{1,6}$, and then increases according to $I_{PL} \sim I_{ex}^{1,8}$ and at high excitation levels PL increases according to the quadratic law $I_{PL} \sim I_{ex}^{2}$. Such behavior of the PL band intensity at 1.51 eV was observed at 90 K in [22]. With an increase in the excitation rate, the spectrum narrows, indicating the onset of a stimulated emission mode, which is confirmed by the superlinear dependence of the emission intensity on pumping. In [8], the authors associate the observed emission line with an energy of 1.53 eV with the resonant annihilation of free excitons.

4. CONCLUSION

$CuInS_2$ crystals were grown by the Bridgman method with slow cooling of melts of stoichiometric composition. The photoluminescence band with a maximum at ~ 811 nm and a half-width of 30 nm was observed at 300 K. It was found that the dependence of the photoluminescence intensity on the intensity of the exciting light is nonlinear.

[1] *L.L. Kazmerski*. Ternary-compound thin-film solar cells. Nuovo Cimento D, 1983, v.2, pp.2013-2018

[2] *R. W. Birkmire, L. C. DiNetta, P. G. Lasswell, J. D. Meakin, and J. E. Phillips*, High efficiency $CuInSe_2$ based heterojunction solar cells: Fabrication and results, Solar Cells, 1986, v.16, pp. 4I9-427.

[3] *C. Rincón, S.M. Wasim, G. Marín, G. Sánchez Pérez, and G. Bacquet.* Temperature dependence of the photoluminescence spectrum of single crystals of $CuInTe_2$. Journal of Applied Physics, 1997, v.82, pp. 4500-4503.

[4] *D. Braunger, Th. Durr, D. Hariskos, Ch. Koble, Th. Walter, N. Wieser, and H.W. Schock*, Improved Voc in $CuInSe_2$-based Solar Cells, in Proceedings of the 25th IEEE Photovotaic Specialists Conference IEEE, New York, 1996, pp.1001.

[5] *J. Klaer, J. Bruns, R. Henninger, K. Siemer, R. Klenck, K. Ellmer, and D. Braunig*, Efficient $CuInS_2$ thin-film solar cells prepared by a

sequential process. Semicond. Sci. Technol. 1998, v.13, p.1456.

[6] *R. Klenk, J. Klaer, R. Scheer, M. Ch. Lux-Steiner, I. Luck, N. Meyer, and U. Ruhle*, Solar cells based on $CuInS_2$—an overview, Thin Solid Films, 2005, v.480/481, pp. 509-514.

[7] *M. Nakamura, K. Yamaguchi, Y. Kimoto, Y. Yasaki, T. Kato, and H. Sugimoto*, "Cd-Free $Cu(In,Ga)(Se,S)_2$ Thin-Film Solar Cell With Record Efficiency of 23.35%," IEEE Journal of Photovoltaics, 2019, v.9, is.6, pp.1863 – 1867.

[8] *B. Tell, J.L. Shay, and H.M. Kasper*. Electrical Properties, Optical Properties, and Band Structure of $CuGaS_2$ and $CulnS_2$, Phys. Rev. B 1971, v.4, pp. 2463–2471.

[9] *J. Gonzalez and C. Rincon.* Optical absorption and phase transitions in $CulnSe_2$ and $CulnS_2$ single crystals at high pressure, Journal of Applied Physics, 1989, v.65, pp. 2031-2034.

[10] *M. Angelov, R. Goldhahn, G. Gobsch, M. Kanis, and S. Fiechter*. Structural and optical properties of $CuInS_2$ bulk crystals, Journal of Applied Physics, 1994, v.75, is.10, pp. 5361-5366.

[11] *L.I. Gurinovich, V. S. Gurin, V. A. Ivanov, I.V. Bodnar, A. P. Molochko, and N.P. Solovej*. "Crystal Structure and Optical Properties of $CuInS_2$ Nanocrystals in a Glass Matrix," Phys.Stat.Sol. (b), 1998. v.208, is.2, pp. 533-540.

[12] *Kenji Yoshino, and Tetsuo Ikari*, Sharp band edge photoluminescence of high-purity $CuInS_2$ single crystals. Applied Physics Letters, 2001, v.78, pp.742-744.

[13] *J.J. M. Binsma, L.J. Giling, and J. Bloem*, Luminescence of $CuInS_2$. J.Lumin. 1982, v.27, pp.55-72

[14] *N. Tsujii, Y. Imanaka, T. Takamasu, H. Kitazawa, and G. Kido*, Photoluminescence of Yb 3+ - doped $CuInS_2$ crystals in magnetic fields Journal of Applied Physics, 2001, v.89, pp. 2706-2710.

[15] *H. Miyake, T. Hayashi, and K. Sugiyama*, Preparation of $CuGa_xIn_{1-x}S_2$ alloys from in solutions, J. Cryst. Growth, 1993, v.134, pp.174-180.

[16] *Kazuki Wakita, Futoshi Fujita, and Nobuyuki Yamamoto*, Photoluminescence excitation spectrum of $CuInS_2$ crystals. Journal of Applied Physics, 2001, v.90, pp.1292-1296.

[17] *Kazuki Wakita, Kazuhito Nishi, Yoshihiko Ohta, and Naoji Nakayama*. Time-resolved photoluminescence studies of free excitons in $CuInS_2$ crystals, Applied Physics Letters, 2002, v.80, pp. 3316-3318.

[18] *L.J. Lim, X. Zhao, Z.-K. Tan*, "Non-Toxic $CuInS_2$/ZnS Colloidal Quantum Dots for Near-Infrared Light-Emitting Diodes," Advanced Materials, 2023, v.35, is.28, p.2301887.

[19] *Sho Shirakata, Akihiro Ogawa, Shigehiro Isomura and Tetsiya Kariya*, Photoluminescence and Photoreflectance of $CuGa(S_{1-x}Se_x)_2$ and $Cu(Ga_{1-x}\ In_x)S_2$ Alloys. Proc.9th Int. Conf. Ternary and Multinary Compounds, Yokohama, 1993, Jpn. J. Appl. Phys. 1993), vol. 32, suppl. 32-3, pp. 94-96.

[20] *H. Neumann*, Lattice vibrations in $A^IB^{III}C^{VI}_2$ chalcopyrite compounds, Helvetica Physica Acta, 1985, v.58, pp.337-346.

[21] *M. V. Yakushev*, Energy of excitons in $CuInS_2$ single crystals, Applied Physics Letters, 2006, v.88, pp. 011922.

[22] *A.I. Dirochka, S.G. Ivanova, L.N. Kurbatov, E.V. Spiitsyn. F.F. Kharakhorin, E.N. Kholina*. Recombination radiation of semiconducting compounds $CuInSe_{1-x}S_x$. Fizika i Technika poluprovodnikov (Sov.j. Semiconductors), 1975, v.9, № 6, pp. 1128-1132.

Received: 28.12.2024

ANALYSIS OF DEPTH PROFILES OF DEFECTS FORMED IN $CuInSe_2$ THIN FILMS AFTER IMPLANTATION WITH Ar^+ IONS

Ch.E. SABZALIYEVA[1], N.N. MURSAKULOV[1,2], Kh.M. GULIYEVA[1], N.N. ABDULZADE[1]

[1]Institute of Physics of the Ministry of Science and Education, H. Javid ave. 131, AZ-1073, Baku, Azerbaijan

[2]Institute of Radiation Problems of the Ministry of Science and Education AZ 1143, B. Vahabzade Ave., 9, Baku, Azerbaijan.

E-mail: ch.sabzaliyeva@mail.ru tel.: +994 538 04 96

Of particular interest is ion implantation of chalcopyrite semiconductor materials $CuInSe_2$ with high conversion efficiency, used as absorber layers in solar cells. $CuInSe_2$ sample was implanted with 30 keV Ar^+ ions at room temperature with an ion current density of 3 μA/cm^2 and a radiation dose ranging from 10^{12} to $3 \cdot 10^{16}$ ions/cm^{-2}. After $3 \cdot 10^{15}$ cm^{-2}, the total damage is calculated to be $3 \cdot 10^{16}$cm^{-2}, suggesting that only 10 out of 525 created defects per implanted Ar ion were left unhealed.

Keywords: ion implantation, chalcopyrite structure, Rutherford backscattering, Gaussian curves.
DOI:10.70784/azip.1.2025113

INTRODUCTION

In recent years, interest in the study of radiation physics of solids has increased significantly. The main reason for this is the search for new types of materials that don't lose their ability to work in high radiation conditions. These materials are used in nuclear technology, space rockets, and the development of detector systems [1]. The lack of sufficient quantities of these new types of materials does not allow for the implementation of large projects. One of the important issues in radiation physics of solids is the study of the effect of various types of radiation on the surface structure of polycrystals and monocrystals.

Chalcopyrite solar cells show high tolerance to irradiation with high-energy electrons or ions, but the origin of this is not well understood. One type of interaction of the surface of a solid with accelerated ions (1-100 keV) is ion implantation [2,3].

The ternary compound $CuInSe_2$ is a semiconductor with a chalcopyrite structure and a band gap of approximately 1 eV. Making drastic changes in the properties of $CuInSe_2$, obtaining solid solutions and new phases based on it are among the development directions of photoelectric converters created based on these materials. Considering that chalcopyrite is a cheap material, this fact is of great interest. $CuInSe_2$ semiconductor materials have high conversion efficiency for photovoltaic devices and a (21.8% for laboratory size thin-film cells) are used as absorber layers for solar cells [4]. $CuInSe_2$ - based solar cells are also resistant to high-energy ion and electron radiation. Rutherford backscattering is an experimental method that provides information about the elemental structure and chemical composition of a substance. Rutherford backscattering spectroscopy is a type of ion scattering spectroscopy that is based on the analysis of the energy spectra of He^+ ions (alpha particles) or protons with energies of~(1–3) MeV scattered in the opposite direction from a sample [5-6]. Rutherford backscattering spectroscopy, like ion scattering spectroscopy, provides information about the chemical composition and crystallinity of a sample, as well as the surface structure of a crystalline sample, according to the energy spectra of the scattered alpha particles depending on the distance from the sample surface (or a certain depth). Combining RBS with the ion channeling effect (RBS/C) by aligning the beam of high energy positive ions with low index axes of the lattice provides information on the near surface depth profile of the concentration of structural defects in the lattice. The well-known energy loss rate (dE/dx) for most materials allows us to move from the energy scale to the depth scale. This is a one-time energy loss in the act of scattering, the amount of which is determined by the mass of the scattering atom [7]. The mechanism of the method is that when the ion beam (alpha particles or protons) is directed along the main directions of symmetry of single crystals, ions that avoid direct collisions with surface atoms can penetrate deep into the crystal (up to hundreds of nm) and move along the channels formed by the atomic rows. By comparing the spectra obtained when the ion beam is directed along the channeling directions and in directions different from them, one can obtain information about the crystalline perfection of the sample under study. From the analysis of the intensity of the surface peak, which is the result of direct collisions of ions with surface atoms, one can obtain information about the structure of the surface, for example, about the presence of reconstructions, relaxations and absorbances [8-9]. From the reflections falling on other energy channels, it is possible to determine the chemical composition. The main feature of the method is to obtain the above information about the sample using high-energy ions that penetrate deep into the solid and are scattered

131, H.Javid ave, AZ-1073, Baku
Institute of Physics
E-mail: jophphysics@gmail.com

back from atoms located deep inside. In this process, the main results are determined by the energy lost by the ion. The scattering cross section is found from the law of conservation of momentum during scattering. Due to the complicated phase diagram, it is difficult to grow $CuInSe_2$ crystals with high structural quality [10-11].

In this study, we have used the Rutherford backscattering technique to study the depth concentrations of defects formed by different doses of 30 KeV Ar ion beam in the Cu, In and Se sublattices of a high-structure quality $CuInSe_2$ single crystal.

EXPERIMENT

From a practical point of view, implantation of $CuInSe_2$ thin layers, which are used as absorber layers in solar cells, with Ar^+ and Xe^+ ions is of great importance.

A single crystal of p-type $CuInSe_2$ with dimensions of 2 × 1 cm and a thickness of 2 mm was grown by the vertical Bridgman method and cut from the middle of the ingot. The sample was mechanically polished with diamond paste. The polished sample was etched in 0.1% bromine methanol solution for 1 min and then heat - treated in vacuum at 300° C to remove the remaining selenium layer on the surface. The orientati on of the crystal was determined using X-ray diffraction patterns before implantation. The sample surface was determined to be within 5° of the (112) plane. After the sample surface was brought to the specified condition, the sample was implanted with 30 keV Ar^+ ions at room temperature with an ion current density of 3 mkA/cm^2 and a radiation dose ranging from 10^{12} to 3 × 10^{16} ions/cm^{-2}. To avoid channeling during implantation, the argon ion beam was positioned approximately 3° from the (221) plane axis used for Rutherford backscattering during implantation. One area was kept unimplanted to be used as a reference (etalon) site [12-13].

RESULTS AND DISCUSSION

The RBS spectra of ternary compounds can be considered as the sum of three separated RBS products corresponding to three atomic species. Each product is shifted in energy scale according to the element mass. In our work, we separate these three products from the overall matched spectrum of $CuInSe_2$. The Rutherford backscattering method was used to obtain depth profiles of the n_{Cu}, n_{In}, and n_{Se} scattering centers in the Cu, In, and Se sublattices, respectively. [14]. The In and Se profiles are shown in Figs. 1(a) and 1(b), respectively. It can be seen from Figure 1 that the concentration profiles of both In and Se consist of two peaks, (P1) a narrow peak at the surface and (P2) a wider peak at a depth of 40 nm. In the In profiles with lower scattering, the shape of these peaks is well described by Gaussian curves. An example of a Gaussian curve corresponding to the depth profile of In atoms after implantation at a dose of 3× 10^{16} ions/cm^{-2} is shown in Figure 1(a). The width of this P1 peak is close to the depth resolution. This means that its shape has changed significantly due to the lack of resolution. Therefore, we propose to explain the P1 peak as a result of the presence of a thin “amorphous” layer. This layer may retain some symmetry, but He^+ ions do not channel within it. The height of this P1 peak does not reach the random value because of a lack of depth resolution. The calculated dependence of the accumulated defects due to P1 on the area of the P1 peak for each dose is shown in Figure 2. It grows almost linearly, without any saturation phenomenon. The second peak (P2) appears in the aligned spectra at a depth of 40 nm after implantation at doses above 1.5 × 10^{15} ions/cm^{-2}.

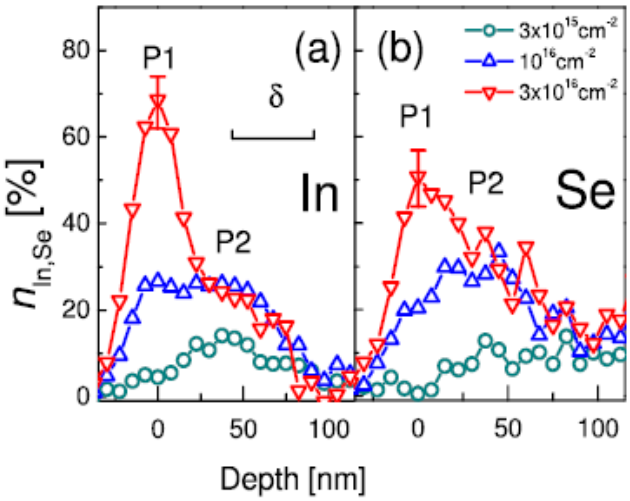

Fig. 1. Depth profiles of n(d) concentrations of scattering centers in the (a) In and (b) Se sublattices after 30 keV Ar^+ implantation.

The intensity of the peak increases with increasing dose and shows saturation at doses above 10^{16} ions/cm^{-2} [15]. The higher resolution for RBS due to indium allows the resolution of the P1 and P2 peaks in the depth profiles of indium, whereas for selenium these peaks merge [16].

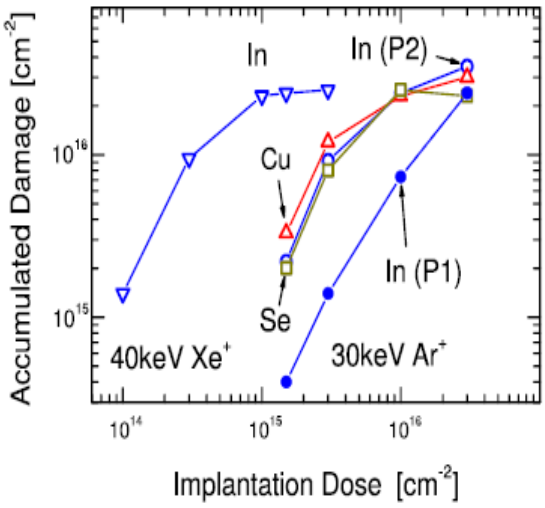

Fig.2. Damage accumulated in Cu, In, and Se sublattices after implantation of $CuInSe_2$ with 40 keV Xe^+ and 30 keV Ar^+ ions.

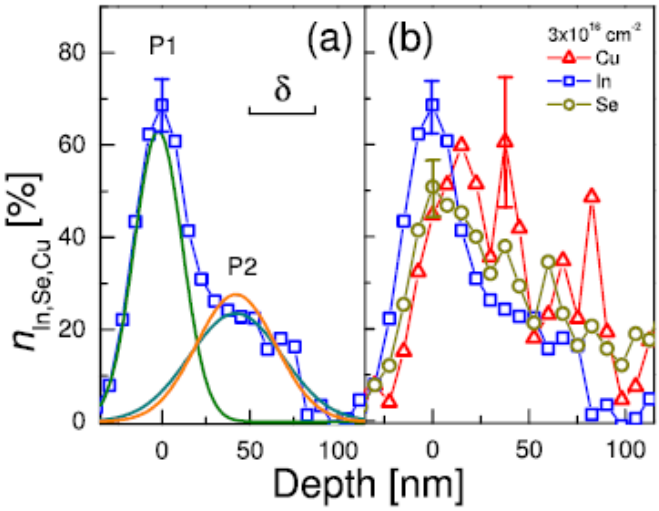

Fig.3. (a) Depth profiles of the In scattering centers after implantation with Ar^+ ions at a dose of 3×10^{16} ion/cm^{-2} (with fitted Gaussians); (b) concentration depth profiles n(d) of the Cu, In, and Se scattering centers after implantation with Ar^+ ions at a dose of 3×10^{16} ion/cm^{-2} (b).

The P2 peaks for different doses of Ar^+ ions are well fitted by Gaussian curves. From Figure 1(a) we see that the deconvolution of this curve leads to a slightly reduced estimate of the full width at half maximum (FWHM) WP2 = 45 nm. The calculated dependences of the accumulated defects related to P2 on the area of the P2 peak for each dose and element are shown in Figure 3. The accumulated damage for all three elements saturate at doses above 3×10^{15} ions/cm^{-2}. The P1 peak can be attributed to the effect of dominant scattering. Using Auger electron spectroscopy, selenium deficiency was detected after sputtering of $CuInSe_2$ single crystals with 5 keV Ar^+ ions. X - ray photoelectron spectroscopy of $CuInSe_2$ single crystals sputtered using 0.5 keV Ar^+ ions revealed the presence of an indium layer with a copper deficient surface of $CuInSe_2$ (the ordered vacancy compound $CuIn_3Se_5$ and the binary phase In_2Se_3) under this layer. The concentration depth profiles and distribution of vacancies induced by irradiation of 30 keV Ar^+ ions in $CuInSe_2$ were calculated using the TRIM program. The average penetration depth and the FWHM of the depth profiles for Ar^+ ions were obtained as R_{Ar} = 27 nm and W_{Ar} = 30 nm, respectively. The calculated depth profiles of vacancies induced by irradiation are slightly smaller, approximately R_{Vac} = 16 nm and FWHM is W_{Vac} = 42 nm [17-18]. The maximum depth of defects is significantly smaller than the experimentally obtained value of R_{P2} = 40 nm. A physical model has been proposed to explain these results. This model is based on the assumption that point defects in $CuInSe_2$ have high mobility at room temperature. This assumption is supported by theoretical calculations of defect formation energies in $CuInSe_2$ and experimental evidence that the implanted copper atoms are very mobile. The mobility of the implanted copper atoms can be enhanced by thermal peaks generated by Ar^+ ions. Theoretical estimates of the thermal effects of 30 keV Ar^+ ions in $CuInSe_2$

predict that the temperature in the volume of the collision cascade can reach 1700 K within 10-11 seconds. We speculate that Ar-implantation can form small bubbles, stacking faults, and dislocation loops [19]. Scanning electron microscopy studies of $CuInSe_2$ crystals implanted with Xe^+ ions revealed high concentrations of stacking faults and dislocation loops [20-21]. According to TRIM calculations, each Ar^+ ion with an energy of 30 keV creates 525 vacancies and interstitial atoms. These defects should amorphize the surface at a distance between 6 nm and 24 nm after a dose of 10^{15} ions/cm^{-2}. However, the first signs of damage are observed in the corresponding aligned spectrum after a dose of 1.5×10^{15} ions/cm^{-2}. This can be considered as evidence for the existence of effective recovery processes at room temperature in $CuInSe_2$. After implantation of 3×10^{15} ions/cm^{-2}, the total defects were calculated to be 3×10^{16} cm^{-3}, which indicates that only 10 out of 525 defects created by each implanted Ar^+ ion remained unrecovered. At first sight, it seems remarkable that 98% of the damage can be self annealed at room temperature. But a more accurate consideration of this effect gives even more interesting results. At this dose, only 10% was calculated to be in the P1 peak, which is associated with dominant scattering, while the rest was found in the P2 peak, which is deeper than the depth predicted by TRIM for unrecovered defects, and this can probably be explained by packing defects and dislocation loops. This indicates that more than 98% of the initial defects recombined and formed defects [22-23].

CONCLUSIONS

Implantation of 30 keV Ar^+ ions into a $CuInSe_2$ single crystal creates two defect layers on the surface, due to sputtering dominated by Se and Cu atoms, and in the implanted Ar layer, probably due to packing defects and dislocation loops. It was found that the way to reduce the implantation of Ar^+ ions into $CuInGa(Se,S)_2$ layers during magnetron sputtering is to make the gas discharge voltage and the seat temperature as small as possible.

[1] *M. Ye.* Electrical Transport Properties and Band Structure of $CuInSe_2$ under High Pressure. M. Ye, R. Tang, Sh. Ma, Q. Tao, X. Wang, Y. Li, and P. Zhu. The Journal of Physical Chemistry. -C 2019, -v. 123, -p. 20757-20761.

[2] *S.J. Yoon.* Structural and Optical properties of Chemically Deposited $CuInSe_2$ Thin Film in Acidic Medium. S. J. Yoon, L. İseul, K. S. Hyung, L. J. Kee, L. H. Young, L. W., H. Sung-Hwan. Journal of Naoscience and Nanotechnology. -2012, -v. 12. № 5. -p. 4313-4316.

[3] *R.A. Young.* The Rietveld Method. R.A. Young. - Oxford: Oxford University Press, - 1993. -p. 290- 298.

[4] *A.V. Mudry, A.V. Korotki, E.P. Zaretskaya, V.B. Zaretskaya, N.N. Mursakulov, N.N.Abdulzade, Ch.E. Sabzaliyeva.* Growth and optical properties of $Cu(In,Ga)Se_2$ thin films on flexible metallic foils. Azerbaijan Journal of Physics volume XVI, Number 2 Series: En June 2010. p.408-413.

[5] *J.L. Shay and J.H. Wernick.* Ternary Chalcopyrite Semiconductors-Growth, Electronic Properties, and Applications (Pergamon, New York, 1975).

[6] *P. Jackson, D. Hariskos, R. Wuerz, O. Kiowski, A. Bauer, T. M. Friedlmeier, and M. Powalla.* Phys. Status Solidi R 9, 28 (2015).

[7] *S.J. Yoon.* Structural and Optical properties of Chemically Deposited $CuInSe_2$ Thin Film in Acidic Medium. S. J. Yoon, L. İseul, K. S. Hyung, L.J. Kee, L. H. Young, L. W., H. Sung-Hwan. Journal of Naoscience and Nanotechnology. -2012, v. 12. № 5. -p. 4313-4316.

[8] *R.A. Young.* The Rietveld Method. R.A. Young. - Oxford: Oxford University Press, - 1993. -p. 290- 298.

[9] *W.K. Chu, J.W. Mayer, and M.A. Nicolet.* Backscattering Spectrometr (Academic, New York/San Francisco/London, 1978).

[10] *T. Haalboom, F. G€odecke, M. Ernst, Ruble, R. Herberholz, and H.W. Schock,* The 11th International Conference Ternary and Multinary Compounds, Institute of Physics, Salford, UK (1997), p. 249.

[11] *M. Yakushev, A. Zegadi, H. Neumann, P.A. Jones, A. E. Hill, R.D. Pilkington, M.A. Slifkin, and R.D. Tomlinson,* Cryst. Res. Technol. 29,427, 1994.

[12] *R.D. Tomlinson.* Sol. Cells 16, 17, 1986.

[13] *M.V. Yakushev, G. Lippold, A.E. Hill, R.D. Pilkington, and R.D. Tomlinson.* J. Mater. Sci.: Mater. Electron. 7, 155, 1996.

[14] *M. Kulik.* Effect of ion implantation on optical properties of near surfaces layers on Kr+ implanted GaAs: SE and RBS investigation. M. Kulik, E. B Asgerov, A. P Kobzev, M. Latek. "Fizikanın müasir problemləri" IX Respublika konfransı. Bakı, -2015, -p. 511-512.

[15] *T.P. Massopust, P.J. Ireland, L.L. Kazmerski, and K.J. Bachmann.* J. Vac. Sci. Technol., A 2, 1123, 1984.

[16] *K. Otte, G. Lippold, D. Hirsch, A. Schindler, and F. Bigl.* Thin Solid Films 361–362, 498, 2000.

[17] *D. Cahen and L. Chernyak.* Adv. Mater. 9, 861, 1997.

[18] *V. Nadazdy, M. Yakushev, E. D. Djebbar, A.E. Hill, and R. D.Tomlinson.* J. Appl. Phys. 84, 4322, 1998.

[19] *P. Sigmund.* Appl. Phys. Lett. 25, 169, 1974.

[20] *C.A. Mullan, C.J. Kiely, M.V. Yakushev, M. Imanieh, R.D. Tomlinson, and A. Rockett.* Philos. Mag. A 73, 1131, 1996.
[21] *J.A. Hinks and S. E. Donnelly.* Philos. Mag. 91, 517, 2011.
[22] *S.E. Donnelly, J.A. Hinks, P.D. Edmondson, R. D. Pilkington, M.Yakushev, and R. C. Birtcher.* Nucl. Instrum. Methods B 242, 686, 2006.
[23] *C. Stephan, S. Schorr, M. Tovar, and H.-W. Schock.* Appl. Phys. Lett. 98,091906, 2011.

Received: 13.01.2025

A SEMICONDUCTOR IS AN ENERGY SOURCE IN THE PRESENCE OF A TEMPERATURE GRADIENT IN AN EXTERNAL ELECTRIC AND MAGNETIC FIELD

E.R. HASANOV[1,2], Sh.G. KHALILOVA[2,1], A.I. ALAKBAROV[2], Z.A. TAGHIYEVA[2], V.M. HAJIYEVA[2], S.A. HUSEYNOVA[2], S.S. AHADOVA[2]

[1]Z. Khalilov str.23, Baku State Uviversity, Baku, Azerbaijan

[2]H. Javid ave., 131, Institute of Physics Ministry of Science and Education of Azerbaijan, Baku, Azerbaijan

In the presence of a temperature gradient $\nabla_x T = const$, an external electric constant field E_0, an external magnetic constant field H_0, an increasing wave is excited in semiconductors with two types of charge carriers and certain deep traps. The frequency values and the increment of the rising wave are determined. It is proved that this unstable wave is excited at a classically strong $(\mu_{\pm} H_0 > c)$ magnetic field. The electric field with increasing wave has a certain value. Analytical formulas are obtained for the oscillation frequency and for the growth increment of the excited wave.

Keywords: frequency, energy source, temperature gradient, impurity semiconductors, an external magnetic field, an external electric field.
DOI:10.70784/azip.1.2025118

INTRODUCTION

In [1], it was shown that hydrodynamic motions in a nonequilibrium plasma in which the temperature gradient is $\nabla T = const$ leads to the appearance of magnetic fields. In the same work, it was found that plasma with a temperature gradient has vibrational properties that are noticeably different from the properties of ordinary plasmas. In the absence of an external field and hydrodynamic motions, "Thermomagnetic" waves are excited in the plasma, in which only the magnetic field oscillates. In the presence of an external permanent magnetic field, the wave vector of thermomagnetic waves should be perpendicular to it and lie in the plane $(\vec{H},\ \vec{\nabla}\mathrm{T})$.

In the presence of an external electric field, a temperature gradient $\nabla T = const$, and hydrodynamic motions $\vec{V}(\vec{r},t)$, the electric current density has the form

$$\vec{J} = \sigma\overrightarrow{E^*} + \sigma'\left[\overrightarrow{E^*}\vec{H}\right] - \alpha\overrightarrow{\nabla T} - \alpha'\left[\overrightarrow{\nabla T}\vec{H}\right] \qquad (1)$$

The electric field E ^ * consists of three parts [1]

$$E^* = \vec{E} + \frac{\left[\vec{V}\vec{H}\right]}{c} + \frac{T}{e}\frac{\Delta\rho}{\rho}, \quad e > 0 \qquad (2)$$

In a solid-state plasma, the conditions for the appearance of thermomagnetic waves were obtained in [2–3]. In impurity semiconductors in the presence of an external constant electric and magnetic field, the conditions for the appearance of unstably recombination waves were studied in detail in [4–6].

In [7], the conditions of internal and external instability in impurity semiconductors were studied theoretically when the ratios of the concentrations of charge carriers are determined as follows

$$\frac{n_-}{n_+} = \frac{v_-}{v_+} \qquad (3)$$

n_+^- is the consensus of electron and hole carriers, v_- is the electron capture frequency and v_+ is the hole capture frequency.

In this theoretical work, we will study the conditions for the appearance of unstable waves inside a semiconductor in the presence of an external electric field, a temperature gradient, an external magnetic field, taking into account hydrodynamic movements, when condition (3) is satisfied.

Basic equations of the problem

Let us consider a semiconductor with two types of charge carriers with singly charged impurity centers with a concentration of N and two multiply negatively charged impurity centers N_-

$$N_0 = N + N_- = const \qquad (4)$$

The continuity equation for electrons and holes in this semiconductor has the form [8]:

$$\frac{\partial n_-}{\partial t} + divj_- = \gamma_-(0)n_{1-}N_- - \gamma_-(E)n_-N_- = \left(\frac{\partial n_-}{\partial t}\right)_{rek} \qquad (5)$$

131, H.Javid ave, AZ-1073, Baku
Institute of Physics
E-mail: jophphysics@gmail.com

$$\frac{\partial n_+}{\partial t} + divj_+ = \gamma_+(E)n_{1+}N - \gamma_+(0)n_+N_- = \left(\frac{\partial n_+}{\partial t}\right)_{rek} \tag{6}$$

$$\frac{\alpha\partial N_-}{\partial t} = \left(\frac{\partial n_+}{\partial t}\right)_{rek} - \left(\frac{\partial n_-}{\partial t}\right)_{rek} \tag{7}$$

$$\Im = e\left(j_+ + j_-\right) \tag{8}$$

$$n_{1-} = \frac{n_-^0}{N_-^0}, \qquad n_{1+} = \frac{n_+^0 N_-^0}{N_0}$$

The sign (0) shows the equilibrium value of the corresponding physical quantities. The electric field (2) in the aforementioned semiconductor has the form

$$\vec{E}^* = \vec{E} + \frac{\left[\vec{V}\vec{H}\right]}{c} + \frac{T}{e}\left(\frac{\nabla n_-}{n^0} - \frac{\nabla n_+}{n_+^0}\right) \tag{9}$$

(T-temperature in ergs).
Current densities are of the form:

$$\overrightarrow{J_+} = \mu_+ n_+ \vec{E}^* + \mu_{1+}\left[\vec{E}^*\vec{H}\right] + \alpha_+\left[\vec{\nabla}T\vec{H}\right] \tag{10}$$

$$\overrightarrow{J_-} = -\mu_- n_- \vec{E}^* + \mu_{1-}\left[\vec{E}^*\vec{H}\right] - \alpha\nabla T - \alpha'_+\left[\vec{\nabla}T\vec{H}\right] \tag{11}$$

THEORY

To obtain the dispersion equation for the current oscillations inside the crystal, it is necessary to solve equations (5,6,7,8) together with (9,10,11). First, we determine the electric field from (8). Substituting $\vec{\Im} = \frac{c}{4\pi} rot\vec{H}$ into (8) we are easily getting

$$\frac{c}{4\pi} rot\vec{H} = \left(\sigma_- + \sigma_+\right)\left[\vec{E}^*\vec{H}\right] + \left(\alpha_+ + \alpha_-\right)\vec{\nabla}T + \left(\alpha'_+ + \alpha'_-\right)\left[\vec{\nabla}T\vec{H}\right], \tag{12}$$

The definition of $\vec{E}$ from (12) is reduced to solving the vector equation

$$\vec{x} = \vec{a} + \left[\vec{b}\vec{x}\right], \tag{13}$$

From (13)

$$\left[\vec{b}\vec{x}\right] = \vec{b}\vec{a} \tag{14}$$

Substitute instead of $\left[\vec{x}\vec{b}\right]$ the right side of his expression $\vec{a} + \left[\vec{b}\vec{x}\right]$ then

$$\vec{x} = \vec{a} + \left[\vec{b}\vec{a}\right] + \vec{b}\left[\vec{b}\vec{x}\right] = \vec{a} + \left[\vec{b}\vec{a}\right] + \vec{b}\left(\vec{b}\vec{a}\right) - b^2 x$$

$$\vec{x} = \frac{\vec{a} + \left[\vec{b}\vec{a}\right] + \left(\vec{a}\vec{b}\right)\vec{b}}{1 + b^2}, \tag{15}$$

Substituting $\vec{a}$ and $\vec{b}$ from (12) in (13), we obtain the electric field of the expression:

$$\vec{E} = -\frac{\left[\vec{V}\vec{H}\right]}{c} - \lambda'\left[\vec{\nabla}T\vec{H}\right] + \frac{c}{4\pi\sigma} rot\vec{H} - \frac{c\sigma'}{4\pi\sigma^2}\left[rotH, \mathrm{H}\right] + \frac{T}{e}\left(\frac{\nabla n_+}{n_+^0} - \frac{\nabla n_-}{n_-^0}\right) + \lambda\nabla T \tag{16}$$

Here $\sigma = \sigma_+ + \sigma_-$, $\lambda = \frac{\alpha_+ + \alpha_-}{\sigma}$, $\lambda' = \frac{\alpha'\sigma_- - \alpha\sigma'}{\sigma^2}$;

$$\alpha' = \alpha'_+ + \alpha'_-; \quad \sigma' = \sigma_{1+} + \sigma_{1-}.$$

The system of equations (5,6,7,8), taking into account (16), determines the dispersion equation for determining the frequency of current oscillations inside the sample. The total current does not depend on the coordinates, but depends on the times $\vec{\mathfrak{I}} = \vec{\mathfrak{I}}(t)$, and with internal instability, the current does not oscillate in the circuit. We will investigate the one-dimensional problem, i.e $\mathfrak{I}'_x = \mathfrak{I}'_x(t) \neq 0.$

$$\mathfrak{I}'_n = \mathfrak{I}'_x = 0, \tag{17}$$

Considering all physical variables in the form of monochromatic waves

$$E = E_0 + E'; \quad n_\pm = n_\pm^0 + n'_\pm, \left(E', n'_\pm\right) \sim e^{i\left(\vec{k}\vec{x} - \omega t\right)}, \; E' << E_0, \quad n'_\pm << n_\pm^0.$$

(k is the wave vector, ω is the oscillation frequency). Determining the current components from (8) after not complicated calculations, we obtain:

$$\mathfrak{I}'_x = \sigma_0 E'_x + E_{0x} + i\sigma_0 k_x L_x E_1 \left(\frac{n'_-}{n_-^0} - \frac{n'_+}{n_+^0}\right) + \sigma_{10} E'_y - 2\frac{\sigma_{10}}{c} V_{0x} H_{0z} + \alpha_0 \gamma \nabla_x T \frac{\vec{E}^*_{0x} \vec{E}^{*'}}{\left(E^*_{0x}\right)^2} \tag{18}$$

$$\mathfrak{I}'_y = \sigma_0 E'_y - \frac{\sigma_0 k_x c}{\omega} E'_y + \frac{\sigma' V_{0x}}{c} H_{0z} - \sigma_{10} \frac{E_{0x}}{H_{0z}} H'_z - \sigma_{10} E'_x - \sigma'_1 E_{0x} - \frac{2\sigma_{10} V_{0y}}{c} H'_z - \frac{\sigma_{10} V_{0z}}{c} H'_y -$$

$$- \sigma_1 E_1 i k_x L_x \left(\frac{n'_-}{n_-^0} - \frac{n'_+}{n_+^0}\right) - \left(\alpha'\right)_0 \nabla_x T = 0 \tag{19}$$

$$\mathfrak{I}'_z = \sigma_0 E'_z - \frac{\sigma_0 k_x c}{\omega} E'_z + \frac{\sigma' V_{0x}}{c} H_{0z} + \sigma_{10} \frac{E_{0x}}{H_{0z}} H'_y - \frac{2\sigma_{10} V_{0z}}{c} H'_z + \frac{\sigma_{10} V_{0z}}{c} H'_z +$$

$$+ \frac{\sigma_{10}}{c}\left(V_y H_y + V_{0z} H'_z\right) = 0 \tag{20}$$

Here:

$$\sigma_0 = \sigma'_{0-} + \sigma'_{0+}, \quad \vec{E}_0 = i\vec{E}_{0x}, \quad \vec{H}_0 = \hbar H_{0z}, \; \sigma' = \frac{d\sigma'^2}{dE_{0x}^2},$$

L_x is length of the sample $H\_y\wedge'$, $H\_z\wedge'$ are the components of the variable magnetic field which are determined from the Maxwell equation

$$\frac{\partial \vec{H}'}{\partial t} = -c \, rot \vec{E}'$$

Defining (19), (20), E'_y and E'_z we put in (18), we easily get:

$$\mathfrak{I}'_x = \sigma_0 u E'_x + e\upsilon + \left[1 + \frac{V_{0y}}{c} - 2\frac{V_{0y}}{c}\beta_{1+}\frac{\mu_{1+}}{\mu_+}\frac{E_1}{E_{0x}} i k_x L_x + \frac{\nabla_x T\left(\alpha_+\gamma_+ - \alpha_-\gamma_-\right)}{E_{0x} n_+ \left(n_+\mu_+ + n_-\mu_-\right)}\right] n'_+ +$$

$$+ e\upsilon - \left[1 - \frac{V_{0y}}{c} + 2\frac{V_{0y}}{c}\frac{\mu_{1-}}{\mu_-}\frac{E_1}{E_{0x}} i k_x L_x + \frac{\nabla_x T\left(\alpha_+\gamma_+ - \alpha_-\gamma_-\right)}{E_{0x} n_+ \left(n_-\mu_- + n_-\mu_-\right)}\right] n'_- \tag{21}$$

Here:

$$u = 2\frac{\sigma_{1+}}{\sigma_0}\frac{V_{0y}}{c}\beta_{1+} + 2\frac{\sigma_{1-}}{\sigma_0}\beta_{1-} + \frac{e\nabla_x T\left(\alpha_+\gamma_+ + \alpha_-\gamma_-\right)}{E_{0x}\sigma_0}$$

$$\beta_{1\pm} = \frac{d\ln\mu_{1\pm}}{d\ln\left(E_{0x}^2\right)}$$

When obtaining (21) from (19),(20) we took into account that $\frac{V_{0y}}{c}H_{0z} << E_{0x}$,

$$\mu_{\pm}E_{0x} << E_{0x}\ \ V_{0y} << c\frac{V_{0y}}{c}$$

We write (21) in the following form

$$E'_x = \frac{\Im'_x}{\sigma_0 u} - \frac{e\vartheta_+\varphi_+}{\sigma_0 u}n'_+ - \frac{e\vartheta_-\varphi_-}{\sigma_0 u}n'_-$$

In [7], it was proved that in the presence of relation (3), equations (5,6,7) have the following form:

$$\begin{aligned}\frac{\partial n'_+}{\partial t} + divj'_+ &= -\nu_+ n'_+ \\ \frac{\partial n'_-}{\partial t} + divj'_- &= -\nu_- n'_-\end{aligned} \tag{22}$$

ν is the electron capture frequency, ν_+ is the hole capture frequency. Having determined from (10-11) $j'_{\pm}$ and substitutingin into (22), then we will obtain the following system of equations for determining the oscillation frequency inside the sample.

$$i\left(k_x\vartheta_+A_+ - \omega\right)n'_+ + \left(A_+ - iA_+ + 2\frac{V_{0y}}{c}\frac{\mu_{1-}}{\mu_-}k_xL_x\right)k_x\vartheta_-n'_- = 0 \tag{23}$$

$$i\left(k_x\vartheta_-A_- - \omega\right)_-n'_- = 0 \tag{24}$$

$$A_+ = \frac{2\sigma_{1+}V_{0y}}{\sigma_0 uc} + \frac{\vartheta_+}{\sigma_0 uL_x};$$

Here,

$$A_- = \frac{2\sigma_{1-}V_{0y}}{\sigma_0 uc} + \frac{\vartheta_-}{\sigma_0 uL_x} \tag{25}$$

$$\vartheta_{1\pm} = \mu_{1\pm}E_1\beta_{1\pm};\quad u = 2\beta\frac{\vartheta_-}{\sigma_0 L_x} + \frac{\alpha\gamma - \nabla_x T}{\sigma_0 E_0}$$

If the scattering of charge carriers comes from one factor (i.e., scattering only from the optical phonon, etc.) then $\beta_{1+} = \beta_{1-} = \beta$. From (18,19) we obtain the following dispersion equations for detect current fluctuations inside the sample

$$\omega^2 - k_x\vartheta\left(A_- + \frac{\mu_+}{\mu_-}A_+\right)\omega + k_x^2\vartheta_-\vartheta_+A_-A_+ - \left(k_x\vartheta_-\right)^2\frac{\vartheta_-}{\sigma_0 L_x u}\left(A_+ + \frac{k_x}{\sigma_{1-}}\vartheta_{1-} - iA_+\right) = 0 \tag{26}$$

Denoting $\frac{\omega}{k_x\vartheta_-} = Z$ from solution (26) we easily obtain

$$Z_{1,2} = \frac{\vartheta_-}{\sigma_0 L_x u}\left[1 \pm \sqrt{\frac{\sigma_0}{n_-^0}} - i\frac{2\mu_{1+}}{\mu_-}\right] \tag{27}$$

$$\sqrt{\frac{\sigma_0}{\sigma_-}} - i\frac{2\mu_{1+}}{\mu_-} = xIy = \frac{1}{\sqrt{2}}\left[\sqrt{1+\frac{4\mu_+^{\ 2}}{\mu_-^{\ 2}}} + 1\right]^{\frac{1}{2}} + i\left[\sqrt{1+\frac{4\mu_+^{\ 2}}{\mu_-^{\ 2}}} - 1\right]^{\frac{1}{2}} = 3/2$$

From (27) it can be seen that a wave with a frequency

$$Z_1 = \frac{\vartheta_-}{\sigma_0 L_x u}(1 + x + iy)$$

$$Z_2 = \frac{\vartheta_-}{\sigma_0 L_x u}(1 - x - iy)$$

is growing, and the wave $\omega_0 = \frac{2k_x \vartheta_-^2}{\sigma_0 L_x u}$, and the growth increment

$$\omega_1 = \frac{3k_x \vartheta_-^2}{2\sqrt{2}\sigma_0 L_x u}, \qquad (28)$$

$$\frac{V_{0y}}{c} = \frac{\vartheta_-}{\sigma_1 - L_x}, \qquad (29)$$

From (27-28) $\frac{\omega_0}{\omega_1} > 1$.

When obtaining (27-28) from (26), it was taken into account that

$$\frac{\mu_+ H_{0z}}{c} = \frac{L_x \sigma_{1-}}{\mu_- E_1} >> 1 \qquad (30)$$

$$E_1 = \frac{2\pi T}{eL_x}$$

(T is the temperature in ergs).

$$L_x >> L_{xar} = \frac{\mu_- E_1}{\sigma_{1-}} \qquad (31)$$

From (29-31) we are getting

$$\frac{\mu_+ H_{0z}}{c} >> \left(\frac{E_1}{eL_x}\right)^2 \qquad (32)$$

DISCUSSION

Thus, in semiconductors with two types of charge carriers, once negatively charged by deep traps and two times negatively charged by deep traps, a wave is excited, which leads to a current oscillation inside the sample. This growing wave is excited when the values of the external magnetic field satisfy condition (32). The electric field in the presence of growing waves, with n_-frequency (32) and increments are determined by expression (33), i.e.

$$E_0 = \frac{2V_{0y}L_x}{c} en_- \frac{\mu_- H_0}{c} \qquad (33)$$

In a crystal of length L_x ~1см, E_0 ~10^3см $\frac{\hat{a}}{\tilde{n}\grave{i}}$.

The frequency is ω_0 ~$3\cdot10^8$(sec)$^{-1}$, the increment is ω_1 ~$3/2\sqrt{2}\cdot10^8$(sec)$^{-1}$. The estimated value of the oscillation frequency inside the crystal is high. When you go outside (that is, the current oscillates in the circuit), you can receive energy radiation from the specified semiconductor. To study the radiation of energy from the above semiconductor, you need to calculate the impedance of the sample.

[1] *L.E. Gurevich.* Journal of Experimental and Theoretical Physics, 1963, 44.

[2] *L.E. Gurevich, V.I. Vladimirov.* Journal of Experimental and Theoretical Physics, 1963, 44, p.166.

[3] *L.E. Gurevich, B.L. Gelmont.* Journal of Experimental and Theoretical Physics, 1964, 46, № 3, p.884.

[4] *A.I. Demirel, E.R. Hasanov and A.Z. Panahov.* Radiations of Electron-Type Conductivity Environments in electric and Magnetic Field Adv. studies Theor.Phys., 2012, vol. 6, № 22, pp. 1077-1086.

[5] *E. Hasanov, A.Z. Panahov, A.H. Demirel.* High Frequency Energy Radiations n-Type Semiconductors at Constant Electric and Magnetic Field Adv. Studiec Theor.Phys., 2013, vol. 7, № 21, p. 1035-1042.

[6] *F.F. Aliev, E.R. Hasanov.* Nonlinear Oscillation Task. For the Consentration of field Carriers in Semiconductors with Deep Traps, IOSR Journal of Applied Physics, (IOSR-JAP), volume10, issue 1, ver.2, 2018, pp. 36-42.

[7] *R.A. Hasanova.* External and Internal Instability in the Medium Having Electron Typ Conductivity IOSR Journal of Applied Physics (IOSR-JAP) vol.10, issue 3, ver. (May-June 2018), pp18-26.

Received: 17.01.2025

ANALYSIS OF THE RESULTS OF STUDYING THE PARTIAL REPLACEMENT OF YTTRIUM BY CADMIUM IN COMPOSITION X

V.M. ALIEV[1], G.I. ISAKOV[1], J.A. RAGIMOV[2], V.I. EMINOVA[3], G.A. ALIEVA[4]

[1]Institute of Physics Ministry of Science and Education of Azerbaijan, AZ 1073, Baku, G. Javid Ave., 131

[2]Azerbaijan Medical University, Baku, AZ 1022, st. Bakikhanova, 23

[3]Azerbaijani-French University under the Azerbaijan State Oil and İndustry University (UFAZ), AZ 1010, Baku, 183 Nizami str.

[4]Institute of National HP Ministry of Science and Education of Azerbaijan AZ 1025, Baku, Khojaly Ave., 30

E-mail: v_aliev@bk.ru

A study was carried out of the effect of substituting Y for Cd on the mechanism of formation of excess conductivity in $Y_{1-x}Cd_xBa_2Cu_3O_{7-\delta}$ (x=0÷1) polycrystals. It is shown that with increasing substitution, the resistivity ρ of the samples increases noticeably, and the critical temperature of transition to the superconducting state Tc decreases.

Increasing the cadmium concentration to x = 0.7, the formation of Cooper pairs (T*) and pseudogap (Δ*(T)) of the samples first increases up to x = 0.5 and then decreases noticeably. We believe that Cd doping creates internal pressure in YBCO, which leads to an observed increase (Δ* (T) due to structural defects.

Keywords: superconductivity, fluctuation conductivity, critical temperature.
DOI:10.70784/azip.1.2025123

1. INTRODUCTION

The works [1-8] analyzed in detail the substitution of yttrium in the composition Y–Ba–Cu–O with rare earth elements (Nd, Tm, Sm, Gd, Er, Yb, La, Dy, Ho, etc.). Note that Y–Ba–Cu–O, despite the maximum number of possible isomorphic substitutions [1–8], is not among the systems where isomorphic heterovalent substitution leads to an increase in the transition temperature Tc. Despite this, the study of substitution in the classical structure of $YBa_2Cu_3O_{7-\delta}$ remains an urgent problem, since it allows us to draw certain conclusions about the mechanism of superconductivity and the contribution of Y, Ba, Cu layers to superconductivity.

However, despite intensive research into HTSCs for more than 30 years, the mechanism of superconducting pairing in such compounds is still highly controversial. It is believed that understanding such an unusual phenomenon as a pseudogap (PG), observed in cuprate HTSCs at T*>>Tc, also allows us to answer the question about the mechanism of SC pairing. But the physics of the appearance of PSH is also not completely clear.

However, the closeness of the ionic radius of yttrium and cadmium gave us the basis to conduct a study on the substitution of yttrium by cadmium in the Y–Ba–Cu–O composition. In this case, we believed that the difference in the ionic radii of Y and Cd leads to a distortion of the YBCO crystal structure. This leads to the formation of defects in the structure and the appearance of pinnings in the crystal structure. The formed pinnings reduce the probability of splitting of Cooper pairs and create the possibility of a HTSC material having a high resistance value in the normal phase transitioning to the superconducting state.

Note that the substitution of yttrium for cadmium in the composition of $YBa_2Cu_3O_{7-\delta}$ HTSC material from 0.1 to 0.7 parts was obtained and analyzed (Fig. 1) [9,10,11].

The presented work is devoted to the study of the above-mentioned substitutions for the normal and SP states of synthesized samples in the temperature range T*>T>Tc, on its influence on their physical characteristics, Δ*(T)). Note that all of the above are $YBa_2Cu_3O_{7-\delta}$ (Y1), $Y_{0,9}Cd_{0,1}Ba_2Cu_3O_{7-\delta}$ (Y2), $Y_{0,7}Cd_{0,3}Ba_2Cu_3O_{7-\delta}$ (Y3), $Y_{0,5}Cd_{0,5}Ba_2Cu_3O_{7-\delta}$ (Y4), $Y_{0,3}Cd_{0,7}Ba_2Cu_3O_{7-\delta}$ (Y5), $Y_{0,1}Cd_{0,9}Ba_2Cu_3O_{7-\delta}$ (Y6) and, $CdBa_2Cu_3O_6$ (Y7), SP composition are discussed in [9, 10, 11].

2. EXPERIMENT

Synthesis and preparation for measurements of polycrystalline compounds $Y_{1-x}Cd_xBa_2Cu_3O_{7-\delta}$ (x = 0.1÷1) is identical to [9,10]. The synthesis of all samples was carried out in two stages.At the first stage, the initial components were mixed in a stoichiometric ratio and annealed in air at a temperature of 1120 K for 25 hours. At the second stage, the resulting compositions were annealed in oxygen (P = 1.2–1.5 atm) at a temperature of 1190 K for 25 hours and slowly cooled to room temperature. The electrical resistance of the samples was measured using a standard four-probe circuit.

3. RESULTS AND DISCUSSIONS

Fluctuation conductivity (FC) for all studied samples was determined from the analysis of excess conductivity σ(T), which was calculated from the difference between the measured resistance ρ(T)

131, H.Javid ave, AZ-1073, Baku
Institute of Physics
E-mail: jophphysics@gmail.com

and the linear normal resistance of the sample $\rho_n(T) = aT + \rho_0$, extrapolated to the low temperature region.

The temperature dependence of the resistivity ρ(T) of the synthesized polycrystals $Y_{1-x}Cd_xBa_2Cu_3O_{7-\delta}$ (x = 0; 0.1; 0.3, 0.5, 0.7) is given in Fig. 1.

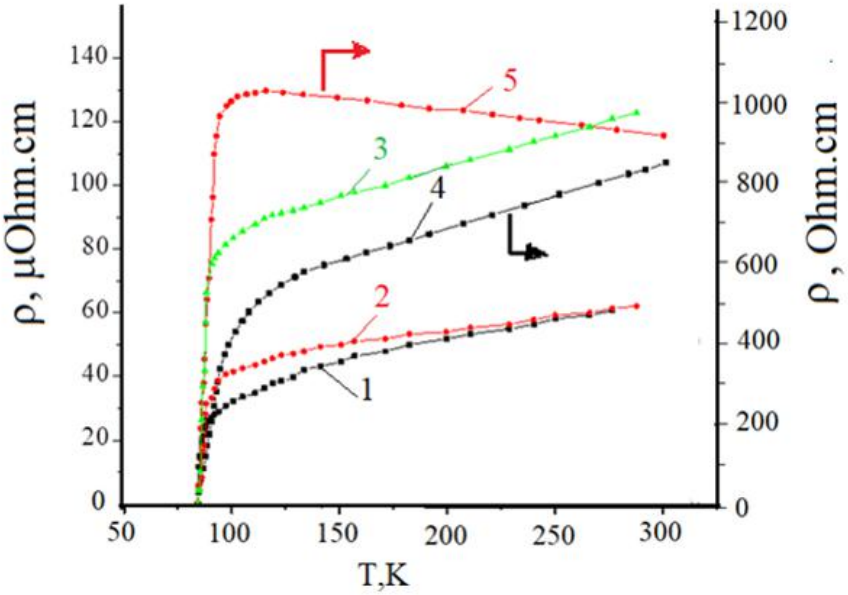

Fig. 1. Temperature dependences of resistivity ρ of polycrystals $Y_{1-x}Cd_xBa_2Cu_3O_{7-\delta}$ at different cadmium concentrations:1(Y1); 2(Y2); 3(Y3); 4(Y4); 5(Y5)

As can be seen in Fig. 1, the critical temperatures of samples of the Y–Ba–Cu–O system when doped with Cd in the case considered remain in the range 84 ~ 87 K. In this case, the resistivity ρ(T) of samples Y1–Y5 in the normal phase at 300 K from Y1 to Y5 increases almost 20 times. Despite the high resistivity, sample Y5 undergoes a SP transition.

We assume that the difference in the ionic radius of Y and Cd leads to a distortion of the YBCO crystal structure. This leads to the formation of defects in the structure and the appearance of pinnings in the crystal structure. The resulting pinning reduces the probability of splitting of Cooper pairs and creates the possibility of transition to the superconducting state of the studied composition, which has a high resistance value in the normal phase.

Note that further increase in substitution of samples, $Y_{0,1}Cd_{0,9}Ba_2Cu_3O_7$ and $CdBa_2Cu_3O_6$ in the normal phase has a semiconductor behavior (Fig. 2). As can be seen from Fig. 2, when the temperature of the samples decreases, it will attempt to make phase transitions of 81 (a) and 173 K (b), respectively. This means that with a change in the synthesis technology, it is possible to obtain SP materials.

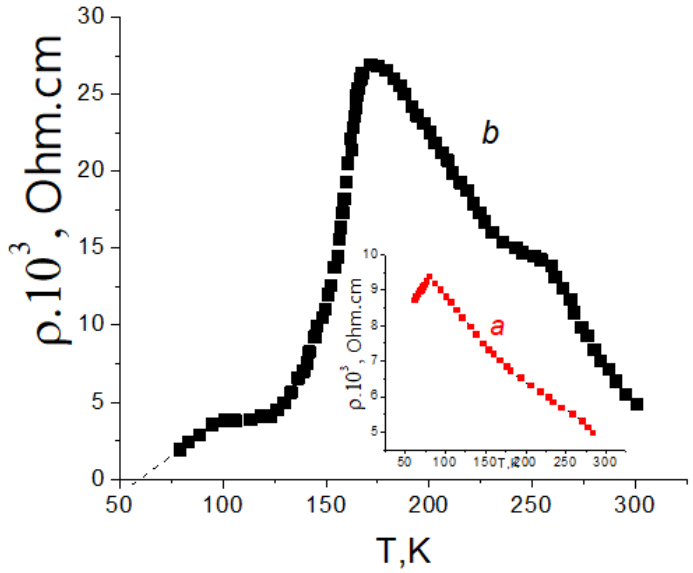

Fig.2. Temperature dependences of resistivity ρ of samples: a- $Y_{0,1}Cd_{0,9}Ba_2Cu_3O_{7-\delta}$ (Y6) and b- $CdBa_2Cu_3O_6$ (Y7)

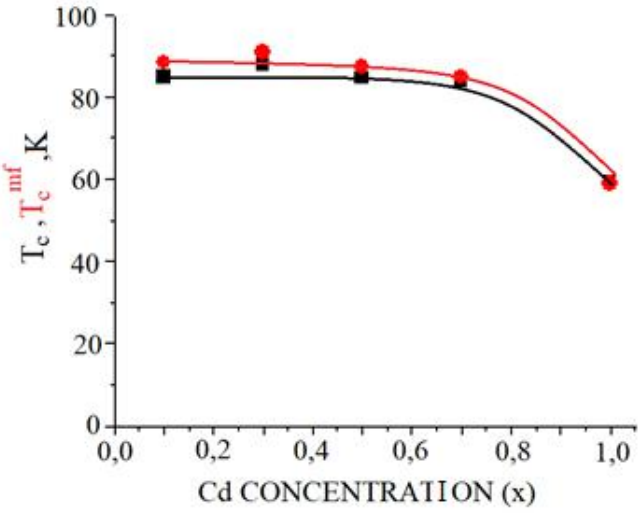

Fig.3. Dependence of T_c (1) andT_c^{mf} (2) of samples $Y_{1-x}Cd_xBa_2Cu_3O_{7-\delta}$ (x=0,1÷0,7)

To carry out fluctuation conductivity of the presented samples within the framework of the LP (local pair) model, it was first necessary to determine the critical temperature in the mean field approximation T_c^{mf}, which separates the FLP region from the region of critical fluctuations. T_c^{mf} - for the analysis of FLP and PS of samples, it is determined from the σ^{-2}–T dependence [12,13].

The research results are presented in Fig. 3.

Analysis of Fig. 3 shows that T_c and T_c^{mf} first (up to 0.3 part substitution of yttrium for cadmium) increases respectively from 88K to 90.7 K and then decreases from 84K to 84.8K.

The temperature at which Cooper pairs begin to form (T*) is an important parameter of both the FLP and the PS, and is also included in all equations. The method for determining T* of samples uses the criterion $[\rho(T)-\rho_0]/aT = 1$, which is obtained by transforming the equation with a straight line [14], where ρ_0 is the residual resistance cut off by this line on the ordinate at T = 0 K. In this In this case, T* is defined as the temperature of the deviation of ρ(T) from 1 [15,16]. The research results for samples Y2–Y5 are shown in Fig. 4.

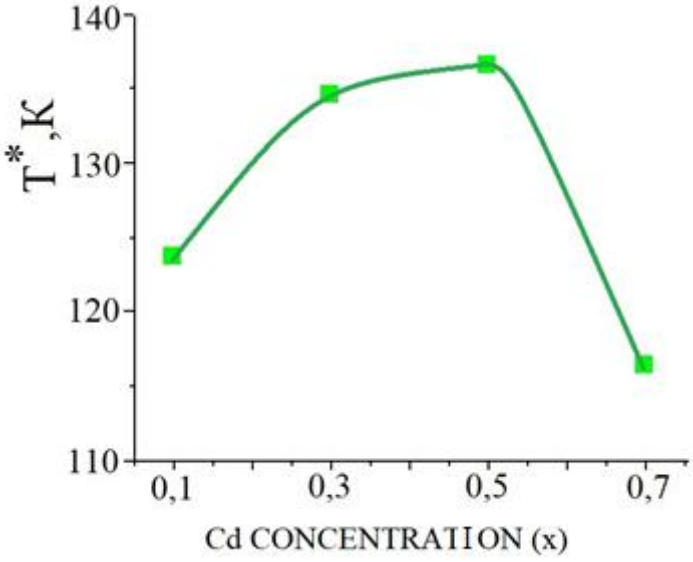

Fig.4. Dependences of pseudogap opening temperature T* for $Y_{1-x}Cd_xBa_2Cu_3O_{7-\delta}$ samples at different concentrations of cadmium (x=0.1÷0.7)

To calculate the temperature dependence of the pseudogap, we used data obtained from the fluctuation conductivity of the $Y_{0.3}Cd_{0.7}Ba_2Cu_3O_{7-\delta}$ HTSC material. An analysis of the magnitude and behavior of the temperature dependence of the pseudogap was presented in the local pair model [17] and further refined in [18] based on the possibility of transition from Bose-Einstein condensation (BEC) to the BCS regime with decreasing temperature in the interval $T^*<T<T_c$ [19].

Note that with decreasing temperature, the value of the pseudogap of the samples first increases, then,

after passing through a maximum, it decreases. This decrease is due to the transformation of FCPs into FCPs (fluctuation Cooper pairs) as a result of the BEC-BCS transition, accompanied by an increase in excess conductivity at $T \rightarrow T_c$[19].

The study of the pseudogap continues to be one of the most relevant areas in the physics of high-temperature superconductors (HTSC) [18]. Despite the large number of accumulated results, both the nature of the PG and the question of its role in the formation of the superconducting state in HTSCs still remain unclear.

The pseudogap phase in HTSCs turned out to be as difficult a problem as high-temperature superconductivity itself. Only key experimental works are discussed and an attempt is made based on their results related to the nature of this unique phenomenon.

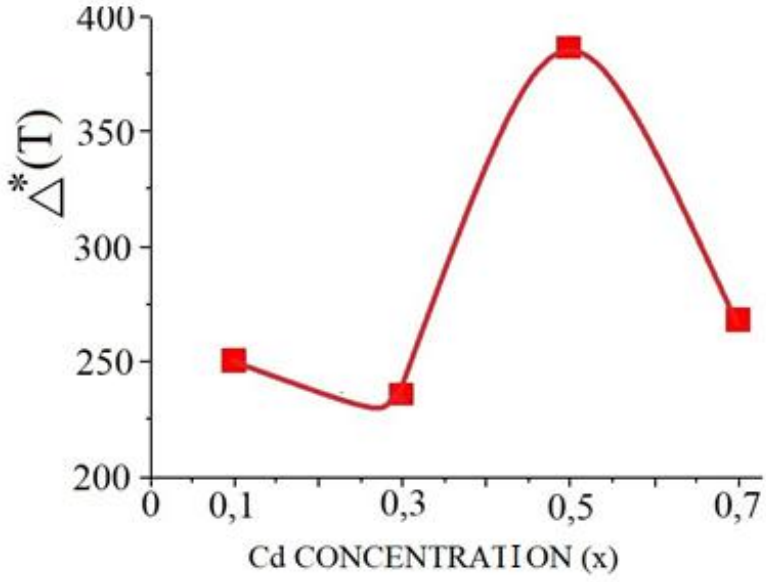

Fig.5. Dependences of the pseudogap (Δ*) of samples $Y_{1-x}Cd_xBa_2Cu_3O_{7-\delta}$ (x=0,1÷0,7)

With an increase in the concentration of cadmium in the sample $Y_{1-x}Cd_xBa_2Cu_3O_{7-\delta}$, the value of the curves (T*) and (Δ*(T) first increases to x=0.5, then decreases noticeably (Fig. 4 and 5). It can be assumed that Cd doping creates an internal pressure in YBCO, which leads to the observed increase due to structural defects. We also assume that a sharp increase in the distance between the conducting planes of CuO_2.

CONCLUSION

A study was carried out of the effect of partial substitution of Y for Cd on the mechanism of formation of excess conductivity and pseudogap in $Y_{1-x}Cd_xBa_2Cu_3O_{7-\delta}$, polycrystals.

Fluctuation conductivity was determined from the analysis of excess conductivity Δσ(T) in Y1–Y5 in the temperature range $T^*>T>T_c$. It was shown that near Tc FLC is well described within the framework of the Aslamazov–Larkin fluctuation theory.

Thus, it can be noted that various defects resulting from Cd intercalation significantly affect the properties of the studied $Y_{1-x}Cd_xBa_2Cu_3O_{7-\delta}$, polycrystals.

[1] *T. Suzuki, T. Yamazaki, and R. Sekine.* J. Mat. Sci. Lett. 8, 381, 1989.

[2] *V.N. Narozhnyi and V.N. Kochetkov. Phys. Rev.* B53, 5856, 1996.

[3] *M. Murakami, N. Sakai, and T. Higuchi*. Supercond. Sci.Technol. 12, 1015, 1996.

[4] *A.L. Soloviev, V.M. Dmitriev*. FNT 33, 32, 2007.

[5] *R.V. Vovk, M.A. Obolensky, A.A. Zavgorodniy, A.V. Bondarenko, M.G. Revyakin.* FNT, 33, 546, 2007.

[6] *L.P. Kozeev, M.Yu. Kamenev, A.I. Romanenko, O.B. Anikeeva, V.E. Fedorov*. Materials 6th International Conference "Crystals: growth, properties, eal structure, application": Alexandrov, September 8–12, 2003, VNIISIMS Publishing House, 2003.

[7] *E.V. Yakubovich, N.N. Oleynikov, V.A. Ketsko, I.V. Arkhangelsky.* Dokl. RAS 386, 502, 2002.

[8] *S. Kambe, G. Samukama, K. Yamaguchi, O. Ishu, I. Shime, T. Nomura, S. Ohshima, K. Okuyama, T. Itoh, H. Suematsu, and H. Yamauchi,* Solid State Phys.108, 283, 1998.

[9] *V.M. Aliev, R.I. Selim-zade, J.A. Ragimov, L.V. Omelchenko, E.V. Petrenko.* FNT, vol. 46, № 9, p. 1068–1077, 2020.

[10] *V.M. Aliev, G.I. Isakov, J.A. Ragimov, R.I. Selim-zade, G.A. Alieva.* Solid State Physics bodies, 65, № 3, p. 404-410, 2023.

[11] *V.M. Aliyev, G.I. Isakov, J.A. Rahimov,*

V.I. Eminova, S.Z. Damirova, G.A. Aliyeva. AJP FIZIKA, vol. X1X № 1, 44-41, 2023.

[12] *A.L. Solovjov.* Superconductors — Materials, Properties and Applications. Chapter 7: Pseudogap and Local Pairs in High-Tc Superconductors, A. M. Gabovich (ed.), Rijeka: InTech, p. 137, 2012.

[13] *B. Oh, K. Char, A. D. Kent, M. Naito, M.R. Beasley, T.H. Geballe, R.H. Hammond, J.M. Graybeal, and A. Kapitulnik.* Phys. Rev. B 37, 7861, 1988.

[14] *E.V.L. de Mello, M.T.D. Orlando, J.L. Gonzalez, E.S. Caixeiro, and E. Baggio-Saitovich.* Phys. Rev. B 66, 092504, 2002.

[15] *V.N. Narozhnyi and V.N. Kochetkov,* Phys. Rev. B 53, 5856, 1996.

[16] *M. Murakami, N. Sakai, and T. Higuchi,* Supercond. Sci. Technol. 12, 1015 (1996).

[17] *V.N. Narozhnyi and V.N. Kochetkov.* Phys. Rev. B 53, 5856, 1996.

[18] *A.L. Solovjov.* Superconductors — Materials, Properties and Applications. Chapter 7: Pseudogap and Local Pairs in High-Tc Superconductors, A.M. Gabovich (ed.), Rijeka: In Tech, p. 137, 2012.

[19] *Прокофьев, М.П. Волков, Ю.А. Бойков.* ФТТ, 45, 1168, 2003.

Received: 17.01.2025

ON THE THEORY OF FREQUENCY DOUBLING IN TWO NONLINEAR CRYSTALS

Sh.Sh. AMIROV[1,2,3], A.I. HASANOVA[1], N.A. MAMMADOVA[1]
[1]Department of Medical and Biological Physics, Azerbaijan Medical University, 167 S.Vurgun str., Az-1022, Baku, Azerbaijan
[2]Faculty of Physics, Baku State University, 23 Z.Khalilov str., Az-1148, Baku, Azerbaijan
[3]Department of Physics and Electronics, Khazar University, 41 Mahsati str., Az-1096, Baku, Azerbaijan
[*]Corresponding author: e-mail: phys_med@mail.ru

The process of frequency doubling in two different nonlinear crystals in series is presented in the constant intensity approximation. The frequency doubling efficiency is sufficiently determined by the phase relationship between interacting waves. Analytical expressions for optimum values of crystal length, phase mismatch and phase relation are obtained in this approximation. It was shown that by choosing the phase mismatch, nonlinear coefficient of coupling for the second crystal unlike from those at the first crystal, as well as the optimum phase condition one can significantly increase the efficiency of frequency doubling in comparison with the identical crystals**.**

Keywords: frequency doubling, constant intensity approximation, phase effects, crystals in series.
DOI:10.70784/azip.1.2025128

1. INTRODUCTION

One of the effective methods of development of powerful sources of coherent radiation in the UV region is the multiplication of laser frequencies. Full conversion of the energy of fundamental wave to the energy of excited one is impossible even in phase matching conditions [1]. To increase coherency length at which occurs the pumping of the energy of exciting wave into the energy of harmonic, in addition to Fabry-Perrot resonators the special schemes including successively placed nonlinear crystals are used [2]. In the fixed field approximation the changes in phases of interacting waves is independent on the intensity of fundamental wave and therefore accurate analysis of the process of nonlinear interaction between waves is impossible. Previously, the constant intensity approximation was applied by us for analysis the second harmonic generation in Fabry-Perrot resonator [3], third harmonic generation in two crystals arranged in series [4] and cascade generation of the third harmonic [5].

2. DISCUSSION AND RESULTS

In this paper we have carried out detailed analysis of the frequency doubling in two series arranged different nonlinear crystals by employing the constant intensity approximation [6].Nonlinear crystals of different lengths are separated with air gap. A pump wave with frequency ω_1 excites the wave with doubled frequency $\omega_2 = 2\omega_1$ in the first crystal. After emergence from the first crystal those waves freely propagate in the air gap and are normally incident onto the surface of the second crystal, where the interaction of propagating waves occurs. One can consider the frequency conversion in each crystal individually. First we write the truncated equations [4,5] describing nonlinear interaction of waves

$$\frac{dA_1}{dz} + \delta_1 A_1 = -i\gamma_1 A_2 A_1^* e^{i\Delta_1 z}$$
$$\frac{dA_2}{dz} + \delta_2 A_2 = -i\gamma_2 A_1^2 e^{-i\Delta_1 z} \quad (1)$$

where $A_j\,(\mathrm{j}=1,2)$ – are the complex amplitudes of a pump and second harmonic waves, waves respectively, δ_j – are the absorption coefficients of those waves, $\Delta_1 = k_2 - 2k_1$ – is the difference in wave numbers (the phase mismatch parameter characterizing deviation from phase matching condition), γ_1, γ_2 – are the coefficients of nonlinear coupling.

Applying boundary conditions $A_1(z=0) = A_{10}$, $A_2(z=0) = 0$ to solve above set of equations in the TCA (most frequently termed as Tagiyev-Chirkin approximation)[6] for a complex amplitude of doubled wave at the exit of the first crystal yields

$$A_2(l_1) = -i\gamma_2 A_{10}^2 l_1 \sin c\lambda_1 l_1 \cdot \exp\left[-\left(\delta_2 + 2\delta_1 + i\Delta_1\right)l_1/2\right] \quad (2)$$

where $\lambda_1 = \left[2\Gamma_1^2 - \frac{\left(\delta_2 - 2\delta_1 - i\Delta_1\right)^2}{4}\right]^{1/2}$, $2\Gamma_1^2 = \gamma_1\gamma_2 I_{10}$, $I_{10} = A_{10}\cdot A_{10}^*$, $\sin cx = \frac{\sin x}{x}$

131, H.Javid ave, AZ-1073, Baku
Institute of Physics
E-mail: jophphysics@gmail.com

A similar expression can be obtained for the complex amplitude of a pump wave at the output of the first crystal

$$A_1(l_1) = A_{10}\left(\cos\lambda_1 l_1 + \frac{\delta_2 - 2\delta_1 - i\Delta_1}{4}\sin\lambda_1 l_1\right)^{1/2} \cdot \exp\left[-\left(\delta_2 + 2\delta_1 + i\Delta_1\right)l_1/4\right] \tag{3}$$

We can obtain from this expression the optimum length $l_1^{opt.}$ of the first crystal at which the harmonic intensity reachs its maximum value:

$$l_1^{opt.} = \frac{arctg(\lambda_1/\delta_2)}{\lambda_1} \tag{4}$$

where $\lambda_1^2 = 2\Gamma_1^2 + \frac{\Delta_1^2}{4}$

The boundary conditions for conversion to second harmonic in the second crystal are given by

$$A_1(z=0) = A_1(l_1)e^{i\varphi_1(d)},\ A_2(z=0) = A_2(l_1)e^{i\varphi_2(d)} \tag{5}$$

where $d-$ is the thickness of air gap between nonlinear crystals, $\varphi_{1,2}(d)-$ are the phase shifts of waves, $z=0$ corresponds to the input of the second crystal.

Analysis of frequency doubling in the second crystal also is carried out by the set of equations (1). However, here we substitute different coefficients for losses, nonlinear coupling as well as difference in wave numbers. Solving new set of equations with boundary conditions (5) for the complex amplitude of second harmonic yields

$$A_{2,out} = A_2(l_1)\left[a - c + (b+u)e^{i\psi} + i(g - fe^{i\psi})\right]\cdot\exp\left[-(\delta_2^{'} + 2\delta_1^{'} + i\Delta_2)z/2\right] \tag{6}$$

where

$$a = \cos\lambda_2 z,\ b = \beta\frac{\lambda_1}{\lambda_2}\cot\lambda_1 l_1\sin\lambda_2 z,\ c = \frac{\delta_2^{'} - 2\delta_1^{'}}{2\lambda_2}\sin\lambda_2 z,\ u = \frac{\delta_2 - 2\delta_1}{2\lambda_2}\sin\lambda_2 z,$$

$$f = \beta\frac{\Delta_1}{2\lambda_2}\sin\lambda_2 z,\ g = \beta\frac{\Delta_2}{2\lambda_2}\sin\lambda_2 z,\ \beta = \frac{\gamma_2^{'}}{\gamma_2}$$

and $\Psi = \Delta_1 l_1 + 2\varphi_1(d) - \varphi_2(d)-$ is the common phase shift between the pump and second harmonic waves in crystals and the air gap.

It is seen from (6) that the amplitude of second harmonic wave is the function of phase shift between Ψ waves. Variation in Ψ is equivalent to the change in signs of coefficients of nonlinear coupling γ_2 and $\gamma_2^{'}$ in the second crystal. Hence, depending on the phase mismatch Δ_2 and coefficients of nonlinear coupling of the second crystal one can distinguish four types of interaction.

Frequency conversion efficiency is given by

$$\eta = \gamma_2\Gamma_1^2(\gamma_1\rho_1)^{-1}(A+B)(\sin^2 x_1\cosh^2 y_1 + \sinh^2 y_1\cos^2 x_2)\times\exp\left[-\left(\delta_2 + 2\delta_1\right)l\right]$$

where

$$A = \left[\cos x_2\cosh y_2 + (Q_5\cos\Psi - Q_6\sin\Psi - \frac{Q_1}{2\sqrt{\rho_2}})\sin x_2\cosh y_2 - (Q_6\cos\Psi + Q_5\sin\Psi + \frac{Q_4}{2\sqrt{\rho_2}})\sinh y_2\cos x_2\right]^2$$

$$B = \left[\left(Q_6\cos\Psi + Q_5\sin\Psi + \frac{Q_4}{2\sqrt{\rho_2}}\right)\sin x_2\cosh y_2 + \left(Q_5\cos\Psi - Q_6\sin\Psi - \frac{Q_1}{2\sqrt{\rho_2}}\right)\sinh y_2\cos x_2 - \sin x_2\sinh y_2\right]^2$$

$$Q_1 = \left(\delta_2^{'} - 2\delta_1^{'}\right)\cos\xi_2/2 - \Delta_1\sin\xi_2/2,\ Q_2 = \left(\delta_2 - 2\delta_1\right)\cos\xi_2/2 - \Delta_1\sin\xi_2/2$$

$$Q_3 = \left(\delta_2 - 2\delta_1\right)\sin\xi_2/2 - \Delta_1\cos\xi_2/2,\ Q_4 = \left(\delta_2^{'} - 2\delta_1^{'}\right)\sin\xi_2/2 - \Delta_1\cos\xi_2/2$$

$$Q_5 = \beta\left(\sqrt{\frac{\rho_1}{\rho_2}}M + \frac{Q_2}{2\sqrt{\rho_2}}\right),\ \ Q_6 = \beta\left(\sqrt{\frac{\rho_1}{\rho_2}}L - \frac{Q_2}{2\sqrt{\rho_2}}\right),\ \beta = \gamma_2^{'}/\gamma_1^{'}$$

$$M = K_1 \cos\theta + K_2 \sin\theta,\ L = K_1 \sin\theta + K_2 \cos\theta,\ K_1 = \frac{\tan x_1 / \cosh^2 y_1}{\tan^2 x_1 + \tanh^2 y_1}$$

$$K_2 = \frac{\tanh y_1 / \cos^2 x_1}{\tan^2 x_1 + \tanh^2 y_1},\ x_{1,2} = \sqrt{\rho_{1,2}}\, l \cos\xi_{1,2}/2,\ y_{1,2} = \sqrt{\rho_{1,2}}\, l \sin\xi_{1,2}/2,$$

$$\rho_{1,2}^2 = \left[2\Gamma_{1,2}^2 + \frac{\Delta_{1,2}^2}{4} - \frac{(\delta_2 - 2\delta_1)^2}{4} \right]^2 + \frac{\Delta_{1,2}^2}{4}(\delta_2 - 2\delta_1)^2,\ \Psi = 2n\pi, \tag{7}$$

$$\xi_{1,2} = \tan^{-1}\left[\Delta_{1,2}(\delta_2 - 2\delta_1)/2\right] \Big/ \left[2\Gamma_{1,2}^2 + \frac{\Delta_{1,2}^2}{4} - \frac{(\delta_2 - 2\delta_1)^2}{4} \right],\ \theta = (\xi_1 - \xi_2)/2$$

Here we apply condition $\delta_2 = 2\delta_1 = \delta$ for losses. Intensity of second harmonic in accordance with (6) can be expressed by

$$I_{2,output} = I_2(l)\left\{a^2 + b^2 + f^2 + g^2 + 2\left[(ab - gf)\cos\Psi + (af + gb)\sin\Psi\right]\right\} \cdot e^{-2\delta l} \tag{8}$$

As can be seen harmonic intensity is a function of parameter Ψ expressing the phase relationship between interacting waves. Efficiency of frequency conversion reaches its maximum, when the following condition is fulfilled:

$$\Psi_{\max} = \pi n + \tan^{-1}\left[\frac{f(a-c) + g(b+u)}{(a-c)(b+u) - gf} \right],\ n = 0,1,2,... \tag{9}$$

Analysis of formula (9) for the optimum value of length of the second crystal yields

$$l_2^{opt.} = \arcsin\lambda_2^{-1}\left(1 + \frac{s}{\sqrt{4+s^2}}\right)/2 \tag{10}$$

where $\Psi = 2n\pi$ and $s^2 = (q^2 + p - 1)/q$, $q = \beta\frac{\lambda_1}{\lambda_2}\cot\lambda_1 l_1$, $p = \frac{(\sigma_2 - \beta\sigma_1)^2}{2 + \sigma_2^2}$, $\sigma_{1,2} = \frac{\Delta_{1,2}}{2\Gamma_1}$.

The phase mismatch parameter receives its optimum value under optimum length of the first crystal:

$$\Delta_2^{opt.} = 4\gamma_1'\Gamma_1\left(\gamma_1\sqrt{2+\sigma_1^2}\right)^{-1} \tag{11}$$

As can be seen from (11) the optimum value of phase mismatch in the second crystal depends not only on the phase mismatch in the first one, but also on the intensity of fundamental wave and coefficients of nonlinear coupling. Taking into account (12) yields to maximum value of harmonic efficiency

$$\eta_{\max.}(\sigma_1) = \frac{1}{2+\sigma_1^2}\left(\frac{\gamma_2}{\gamma_1} + \frac{1}{2}\frac{\gamma_2'}{\gamma_1'}\sigma_1\sqrt{2+\sigma_1^2}\right) \tag{12}$$

From (12) it follows that to obtain maximum efficiency of second harmonic the phase mismatch Δ_1 in the first crystal should receive definite $(\Delta_1 \neq 0)$ value. Further increase in phase mismatch Δ_1 leads to saturation in harmonic efficiency.

3. CONCLUSION

Analysis of frequency doubling in the Tagiyev-Chirkin approximation has allowed us to consider influence of the phases of backward waves on the phase of pumping wave as well as the linear losses of the interacting waves in the nonlinear medium. At the optimum crystal length the frequency doubling efficiency reaches its maximum value depending on both the intensity and the linear losses of the interacting waves. Optimim values of parameters such as crystal length, phase mismatch and phase relationship obtained in the mentioned approximation are the functions of intensity of fundamental wave. With the purpose to

increase efficiency of frequency doubling more suitable type of conversion is considered to be with the same signs of nonlinear coupling coefficients and opposite signs of phase mismatch parameters. Thus by choosing the optimum values of problem parameters and compensating undesired phase shifts of interacting waves one can increase efficiency of conversion upon second harmonic generation in different nonlinear crystals arranged in series.

---

[1] *J.F. Rayntjes.* Nonlinear Optical Parametrical Processes in Liquids and Gases (in Russian) Moscow, Mir, 1987 , 512 p.

[2] *H. Huang, H. Wang, Sh. Wang and D. Shen.* Designable cascaded nonlinear optical frequency conversion integrating multiple nonlinear interactions in two $KTiAsO_4$ crystal. Optics express. 2018, V.26, issue 2, p.642-650.

[3] *Z.A. Tagiev, R.J. Kasumova and Sh.Sh. Amirov.* Theory of Intracavity Second Harmonic Generation in the Fixed-Intensity Approximation (in Russian). Opt. Spectrosk.1993, v.75, issue 4, pp.908-913.

[4] *Z.A.Tagiev and Sh.Sh. Amirov.* Third Harmonic Generation in nonlinear crystals arranged in series (in Russian) . Opt.Spectrosk.1992, v.73, issue 3 , pp.578-582.

[5] *Sh.Sh. Amirov, Z.A. Tagiev, M.G. Shakhtakhtinsky.* On the Theory of Cascade Third Harmonic Generation (in Russian).Quantum Electronics 1991, v.18, issue 6, pp.715-717.

[6] *Z.A. Tagiev and A.S. Chirkin.* Fixed intensity approximation in the thory of nonlinear waves id dispersed media (in Russian). Zh.Eksp. Teor.Fiz. 1977, v.73, issue 4, pp.1271-1282.

Received: 30.01.2025

STRUCTURAL AND MORPHOLOGICAL CHARACTERIZATION OF HIGHLY ALIGNED FERROMAGNETIC PVDF/Fe_3O_4 NANOCOMPOSITE COATING

DILARA SADIGOVA[1], RASIM JABBAROV[2]

[1]Nanotechnology Laboratory. Department of Chemical Engineering, School of Science and Engineering, Khazar University, Baku Azerbaijan

[2]Institute of Physics Ministry of Science and Education of Azerbaijan.

**e-mail: dilara.sadigova3377@gmail.com*

***e-mail: rasim.jabbarov69@gmail.com*

PVDF is a semi-crystalline fluoropolymer and has attracted a lot of interest in a variety of industrial applications because of its special qualities, which include thermal stability, chemical resistance, and piezoelectricity. A polar phase is present in the β-phase. Sensors, actuators, energy harvesting systems, batteries, filters, chemical warfare defense, magnetoelectric, and polymer-based composites were among the many applications it was found to have. In this work, the β-phase fraction of the PVDF/Fe_3O_4 nanocomposite was measured by X-Ray diffraction analysis.

Keywords: PVDF; Fe_3O_4; X-ray diffraction; β-phase; nanocoating; high electroactive phase; electrospinning;
DOI:10.70784/azip.1.2025132

INTRODUCTION

PVDF is a thermoplastic fluoropolymer that is extremely nonreactive and is made by polymerizing vinylidene difluoride. It can display effective ferroelectric, pyroelectric, and piezoelectric qualities following poling process treatment [1,2]. The four crystalline phases α, β, γ, and δ are observed based on the chain configuration of PVDF. resistance [3, 4–8]. The δ-phase is ferroelectric and possesses a polar phase. The α phase also has polar counterparts in the β and γ. Since they are affordable and have chemical resistance and biocompatibility, they are widely used in sensors, actuators, energy harvesting systems, batteries, filters, chemical warfare protection, magnetoelectric, and polymer-based composites [9-11]. In PVDF, the β-phase is distinguished by the highest spontaneous polarization and a certain chain shape per crystal unit cell. A number of processes have been thoroughly investigated in order to reveal the more electroactive β-phase in PVDF, involving phase transition, solvent casting, nucleating fillers, electrospinning, and copolymerization of PVDF [3, 12-15]. In the past decade, a lot of effort has been made to use the electrospinning technology to create fibers in the submicron range due to its higher quality and versatility [16,17]. Feeding the solution and applying a high voltage between the nozzle and collector stretches is necessary for the electrospinning setup, which turns the fluid into nanofibers. The conversion of the PVDF nanofibers from their mainly α-phase to their β-phase can be influenced by a number of electrospinning process factors. The conversion of the PVDF nanofibers from their mainly α-phase to their β-phase can be influenced by a number of electrospinning process factors [18]. In order to boost the β-phase in the produced PVDF nanofibers, a number of experiments have been conducted to optimize these characteristics. Several of the eight previously listed characteristics have been taken into account in the majority of these investigations [19]. The impact of various solvent ratios, flow rate, spinning distance, and electrospinning voltage on the β-phase fraction was examined in a study by Gee et al. [20], the effect of DMF and acetone ratio, flow rate, spin distance and working temperature on the fraction of β-phase was studied. The impact of DMF and acetone ratio, flow rate, spin distance, and working temperature on the proportion of β-phase was examined in another parameter study conducted by Zheng et al. [21]. Yee et al. conducted a second investigation to examine the impact of DMF and acetone ratios on the β-phase fraction [22].

Applications for PVDF-based hydrophobic surfaces include anti-icing, sensing, pollution control, water treatment, oil-water separation, medicinal, and self-cleaning. Research into renewable resources, environmentally friendly solvents, and longer-lasting surface components is necessary for the sustainable production of PVDF nanocomposite materials. To handle trash from nanocomposite materials in an efficient and ecologically conscious way employing cutting-edge techniques like chemical and biological recycling, ongoing research is required.

In this work by using electrospinning equipment is gained highly aligned nano-magnetically enable PVDF-Fe_3O_4 composite material for icephobic applications. Poling of PVDF was carried out to increase β-phase and an aligned molecular structure by using electric and magnetic field stretching at the same time as mechanical stretching forces.

MATERIALS AND METHODS

Materials

Polyvinylidene fluoride (PVDF) pellet has Mw = 1.8 × 104 with linear chemical structure $(-CH_2CF_2-)_n$ were pouched from Sigma-Aldrich, Fe_3O_4 was obtained from Sigma-Aldrich with an average particle size of 20-30 nm. Acetone and N, N-dimethylformamide (DMF) were purchased from Sigma-Aldrich, Polysorbate Tween purchased from Sigma-Aldrich, Strong magnet, Metal bar

131, H.Javid ave, AZ-1073, Baku
Institute of Physics
E-mail: jophphysics@gmail.com

Preparation of solutions

PVDF powders were dissolved in a mixture of organic solvents (DMF/acetone = 1/1 at 10 weight percent (w/w)) using a magnetic stirrer at a maximum temperature of 35˚C for two hours at 35 rpm in a 250 ml beaker. Once the powders were fully dissolved, the Ultrasonic Cleaner Digital Pro was used for two hours to create a homogenous PVDF solution free of bubbles.

Initially, 50 milliliters of DMF were used to dissolve the Fe_3O_4 nanoparticle powders, and 10 milliliters of Polysorbate Tween were added as a surfactant. The mixture was then stirred at 35 rpm for two hours at 30 degrees Celsius to create a solution with a 1 weight percent concentration. After that, sonication was done for two hours to obtain a non-homogenous solution. A two-phased solution was created following ultrasonication, and the electrospinning process used the top phase. Stretching the nanofibers using a mechanical force can organize the lamellae to create fibers aligned along the fiber axis and provide elongation forces during electrospinning [23].

In this study, mechanical stretching forces were achieved by simultaneously using electric and magnetic field stretching.

Preparation PVDF/Fe_3O_4 mats by electrospinning

The PVDF-Fe_3O_4 composite material was made by increasing the speed of the rotating drum while only electrical field stretching was present. The parameters were 3000 rpm, 13 kV voltage, flow rates of 5 ml/hr for PVDF and 0.5 ml/hr for Fe_3O_4. The polymer and Fe_3O_4 solution were fed into a dual channel programmable syringe pump, with each channel being independently controlled. The PVDF solution was electrospun at 13 kV voltage in a plastic syringe with a 20G needle. The PVDF solution flowed at 5 milliliters per hour. Five centimeters separated the collector and needle. A tubeless plastic syringe that was attached directly to the needle was used to inject the Fe_3O_4 solution, saving money on costly nanoparticle material. The same syringe pump was used to inject Fe_3O_4 solution into the syringe with a second 20G needle in order to create a magnetic field. 0.5 ml/h was the magnetite solution's flow rate. Figure 1 described the experimental setup. Using magnetic stretching to increase the alignment and crystallinity of PVDF could improve its wettability and icephobic properties. A strong magnetic field was attached to the electrospinning equipment's grinding line using a metal bar to create a magnetic field, and some magnetit (Fe_3O_4) molecules were drawn to the strong magnetic field. PVDF and Fe_3O_4 solutions are injected onto the surface of the rotary drum. Since the Fe_3O_4 molecules are attracted to the strong magnetic field, a small amount of the injected Fe_3O_4 solution forms a thin thread between the magnetite syringe and the strong magnet, and the PVDF material is mechanically stretched by the magnetic field. PVDF and Fe_3O_4 solutions are injected onto the surface of the rotary drum. Since the Fe_3O_4 molecules are attracted to the strong magnetic field, a small amount of the injected Fe_3O_4 solution forms an extremely thin thread between the magnetite syringe and the strong magnet, and the PVDF material is mechanically stretched by the magnetic field.

RESULTS AND DISCUSSION

Microscopic and Morphological structure analysis

Microscopic analysis. Figure 2 displays microscopic analysis demonstrating the size and shape of the PVDF nanofibers. 10 kV was the acceleration voltage used in SEM imaging. The nanofibers made from 10% PVDF have a consistent shape devoid of twisting and beading patterns. Representative SEM micrographs of morphologically homogeneous surfaces taken at 1000–25,000 times magnification are displayed in Figure 2.

The PVDF/Fe_3O_4 nanofiber material's highly aligned structure is seen in the SEM image with only a 10 µm scale bar (see fig. 2b)). These numbers show the development of ultrafine fibers with a diameter between 134 and 411 nm. Figure 3 shows that the fiber's average diameter is 224 nm. The fiber's average diameter is 224 nm. Electrospun nanofibers had a columnar shape and were consistent in morphology. Fe_3O_4 nanoparticles are dispersed in twisting configurations on the PVDF/Fe_3O_4 nanofiber coating, as demonstrated by the 10 µm picture, which was created by electrospinning with just a metal bar. A highly aligned sample was used to conduct additional research on PVDF/Fe_3O_4 nanofiber coating for spectroscopic examination.

X-Ray diffraction analysis (XRD). The phases of different PVDF polymeric systems have been validated and identified using X-Ray diffraction analysis (XRD) data because XRD makes it easy to distinguish between the electroactive β phase and the nonelectroactive α phase. The produced samples were subjected to XRD examination using a Rigaku Mini Flex 600 XRD diffractometer. Using a Cu X-ray tube operated at 15 mA and 30 kV, CuK(a) radiation was employed for every case. The PVDF/Fe_3O_4 nanocomposite was examined by X-ray diffraction investigation at room temperature, 25°C. Figure 4c) shows X-ray diffractogram of PVDF/Fe_3O_4 nanocomposite with 10 wt% concentration. Figure 4a), Figure 4b) are the data preparation steps for Figure 4c). Red curve indicates PVDF, black curve indicates Fe_3O_4 diffraction area. Red Curve (Lowest Intensity) shows a broad peak at lower angles, suggesting an amorphous or semi-crystalline phase. The intensity is relatively low, indicating a lower level of crystallinity. Black Curve (Highest Intensity) contains multiple sharp peaks, characteristic of a highly crystalline material. Blue Curve (Intermediate Intensity) displays a combination of broad and sharp peaks and indicates a mixture of crystalline and amorphous phases. Some sharp peaks suggest the presence of crystalline domains. Diffraction patterns were obtained in the range of Bragg's angle in a range: 5° - 100°. All diffraction peaks ($2\theta = 19^{\circ}$, 21°, 25°, 39°, 45°, 66°, 79°) are duly indexed from the JCPDC (Joint Commite on Powder Diffraction Standards). Strong diffraction peaks for $2\theta = 21^{\circ}$, 39°, 45°, 66°, 79° assigned to β crystal phase of PVDF and lattice planes

of Fe_3O_4 crystal with the cubic spinal structure. Weaker diffraction peaks for 2ɵ =19°, 25° attributed to the 020, 021 reflections of the monoclinic α crystal phase. The main X-ray peaks of Fe_3O_4 solution were observed at 39º, 45º, 66º, 79º which correspond to (311), (400), (440) and (444) are reflects to Fe_3O_4 crystal with the inverse cubic spinal structure.

The discussion in this work concentrates on the crystalline phase**,** especially on the most common α**,** β phases. As shown in XRD characterization figure 4c), the PVDF solution is mainly made of the β phase as evidenced by a strong peak at 21° corresponding to 110 reflection of the orthorhombic β phase. Presence of high intense peak at 21° confirms the presence of β-phase in PVDF film. Due to the medium electric voltage (13 kV) used during the electrospinning method, the random electric dipoles in the PVDF solution aligned, resulting in the forming of the β phase crystal structure. These results indicated that electrospun nanofiber membranes contain mainly β-phase crystal structure of PVDF.

CONCLUSIONS

In this study, we synthesized PVDF/Fe_3O_4 nanocomposite material, and the SEM pictures show that the aligned nanofibers were produced using the electrospinning technique. Using a directional electric field in electrospinning equipment, we obtained highly aligned nanofibrous film material to investigate their morphology structure. X-Ray diffraction analysis (XRD) was used to validate and identify the phases of PVDF polymeric systems, and the XRD analysis revealed that the PVDF solution is primarily composed of the β phase. These findings suggest that electrospun nanofiber membranes contain primarily the β-phase crystal structure of PVDF.

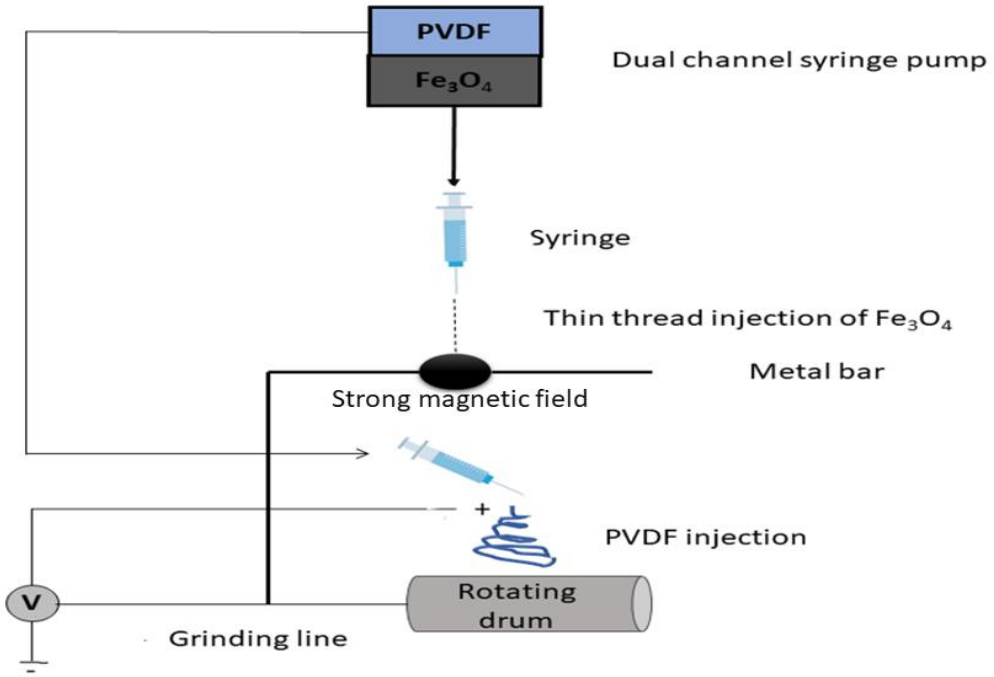

Fig. 1. Experimental set-up of electrospinning.

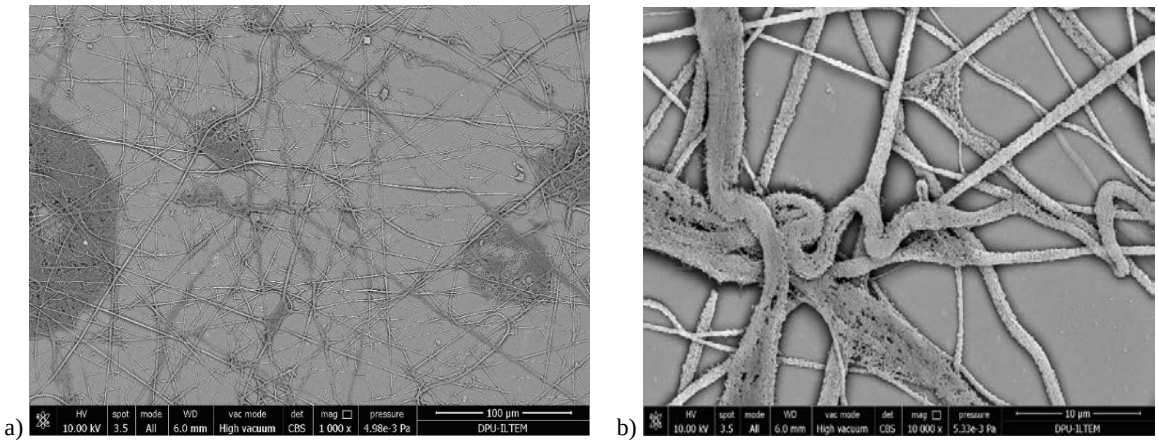

Fig. 2. SEM images of PVDF/Fe_3O_4 nanofiber sample (Rotating Drum speed=3000 rpm; Voltage-13 kV) at a) 100 µm, b)10 µm image.

	Label	Area	Mean	Min	Max	Angle	Length
1		0.005	154.259	65.167	190.984	-4.399	0.192
2		0.010	179.698	81.000	203.424	-53.746	0.411
3		0.003	196.690	110.000	219.333	-99.462	0.134
4		0.004	168.778	119.000	196.250	-172.875	0.178
5		0.005	188.078	147.000	203.333	-49.399	0.204
6		0.004	187.556	171.000	203.000	-90.000	0.177
7		0.007	186.102	125.000	206.408	-39.289	0.314
8		0.006	168.282	36.000	200.250	-131.634	0.266
9		0.005	219.182	155.000	246.000	-90.000	0.221
10		0.005	189.785	114.000	223.000	-36.870	0.221
11		0.005	189.219	124.000	208.667	-139.399	0.204
12		0.004	179.804	123.000	201.000	-105.945	0.161
13	Mean	0.005	183.953	114.181	208.471	-84.418	0.224
14	SD	0.002	16.216	38.042	14.778	49.264	0.076
15	Min	0.003	154.259	36.000	190.984	-172.875	0.134
16	Max	0.010	219.182	171.000	246.000	-4.399	0.411

Fig. 3. Calculation average length size (diameter) of PVDF/Fe_3O_4 nanofiber.

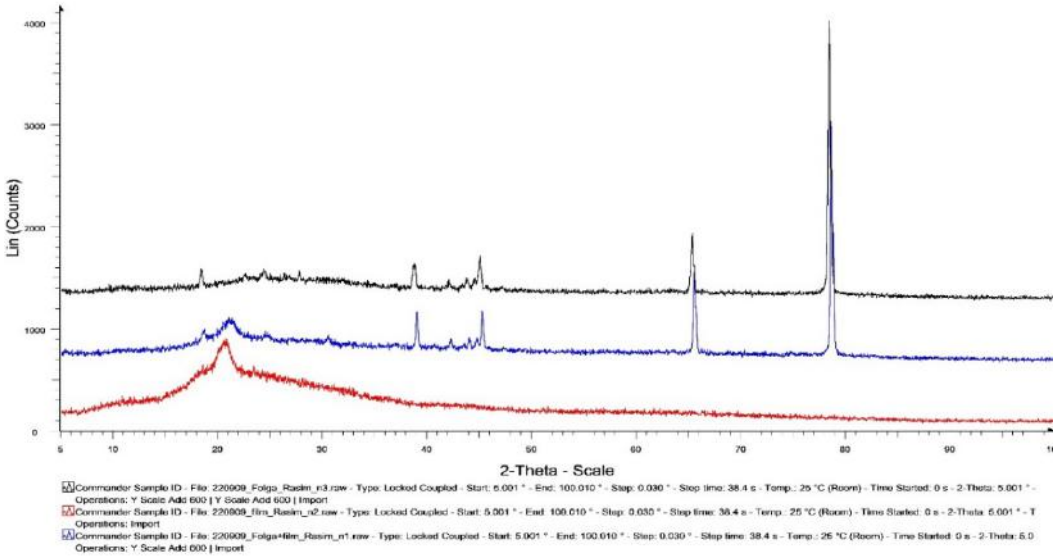

a)

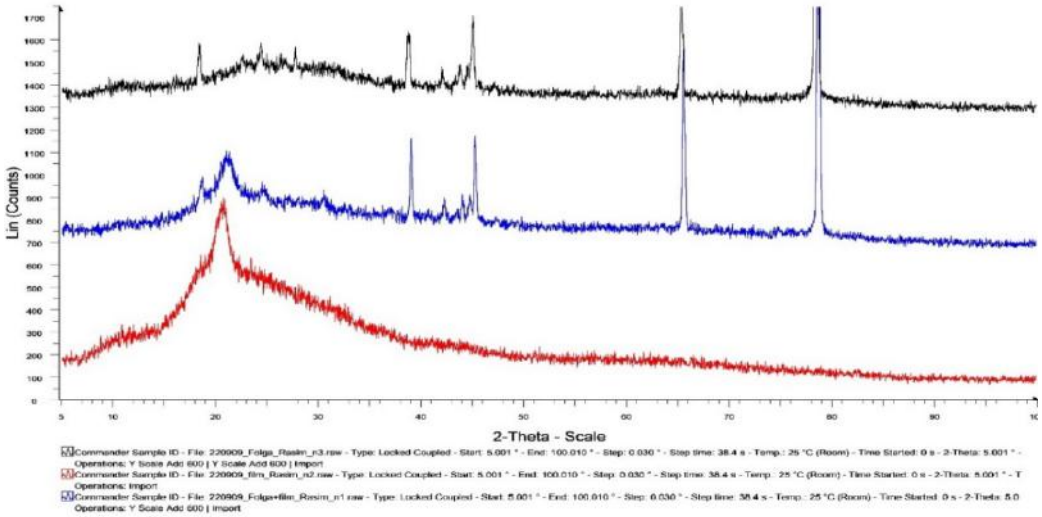

b) X-ray diffraction pattern of PVDF/ Fe_3O_4 nanofiber.

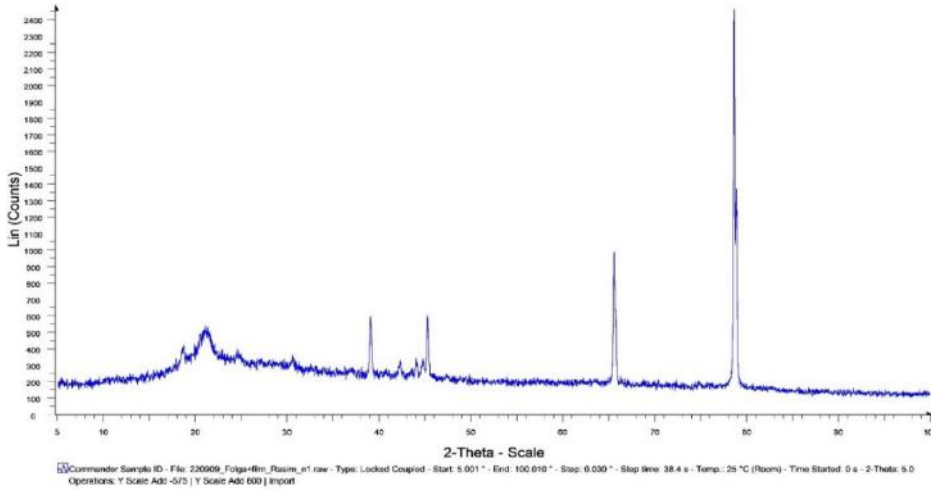

c)

Fig. 4. Data preparation steps of X-ray diffraction pattern of PVDF/ Fe_3O_4 nanofiber: 4a), 4b); X-ray diffraction pattern of PVDF/ Fe_3O_4 nanofiber: 4c).

[1] *S. Lanceros-Me´ndez, P. Martins.* First Ed., Magnetoelectric Polymer-Based Composites Fundamentals and Applications Wiley, Germany 2017.

[2] *P. Ueberschlag.* Sens. Rev. 21, 118, 2001.

[3] *S. Bauer, F. Bauer.* Springer Ser. Mater. Sci. 157 2008.

[4] *Z.W. Ouyang, E.C. Chen, T.M. Wu.* Materials 8, 4553, 2015.

[5] *A.J. Lovinger.* Science 220, 1115, 1983.

[6] *V. Sencadas, R.G. Filho, S. Lanceros-Mendez.* J. Non-Cryst. Solids 352, 2226, 2006.

[7] *G. Botelho, S. Lanceros-Mendez, A.M. Goncalves, V. Sencadas, J.G. Rocha, J. N G.T. Davis, J.E. McKinney, M.G. Broadhurst, S.C. Roth.* J. Appl. Phys. 49, 4998, 1978.

[8] *N. Levi, R. Czerw, S. Xing, P. Iyer, D.L. Carroll.* Nano Lett. 4, 1267, 2004.

[9] *J.Y. Lim, J. Kim, S. Kim, S. Kwak, Y. Lee, Y. Seo.* Polymer 62, 11, 2015.

[10] *A.S. Motamedi, H. Mirzadeh, F. Hajiesmaeilb, J. Xu, M.J. Dapino, D. Gallego-Perez, D. Hansford.* Sens. Actuators A 153, 24, 2009.

[11] *P. Martins, A.C. Lopes, S. Lanceros-Mendez.* Prog. Polym. Sci. 39, 683, 2014.

[12] *S. Harstad, N. D'Souza, N. Soin, A.A. El-Gendy, S. Gupta, V.K. Pecharsky, T. Shah, E. Siores, R.L. Hadimani.* AIP Adv. 7, 056411, 2017.

[13] *L. Ruan, X. Yao, Y. Chang, L. Zhou, G. Qin, X. Zhang.* Polymers 10, 1, 2018.

[14] *Y.C. Ahn, S.K. Park, G.T. Kim, Y.J. Hwang, C.G. Lee, H.S. Shin, J.K. Lee.* Curr. Appl. Phys. 6, 1030 2006.

[15] *C. Ribeiro, V. Sencadas, J.L.G. Ribelles, S. Lanceros-Méndez.* Influence of processing conditions on polymorphism and nanofiber morphology of electroactive poly(vinylidene fluoride) electrospun membranes. Soft Mater. 8, 2010, 274–287.

[16] *S. Ramakrishna, K. Fujihara, W. Teo, T.-C. Lim, Z. Ma.* An Introduction to Electrospinning and Nanofibers; World Scientific Publishing Company: Singapore, 2005

[17] *A. Haider, S. Haider, I.-K. Kang.* A comprehensive review summarizing the effect of electrospinning parameters and potential applications of nanofibers in biomedical and biotechnology, Arab. J. Chem. 11 (2018) 1165–1188.

[18] *Rahul Kumar Singh, Sun Woh Lye, Jianmin Miao*. Holistic investigation of the electrospinning parameters for high percentage of β-phase in PVDF nanofibers Polymer 214 (2021) 123366.

[19] *S. Gee, B. Johnson, A. Smith.* Optimizing electrospinning parameters for piezoelectric PVDF nanofiber membranes, J. Membr. Sci. 563 (2018) 804–812.

[20] *J. Zheng, A. He, J. Li, C.C. Han*. Polymorphism control of poly (vinylidene fluoride) through electrospinning, Macromol. Rapid Commun. 28 (2007) 2159–2162.

[21] *W.A. Yee, M. Kotaki, Y. Liu, X. Lu.* Morphology, polymorphism behavior and molecular orientation of electrospun poly (vinylidene fluoride) fibers, Polymer 48 (2007) 512–521.

[22] *Zhou, Z.;Wu, X.-F.* Electrospinning superhydrophobic-superoleophilic fibrous PVDF membranes for high-efficiency water-oil separation. Mater. Lett. 2015, 160, 423–427.

Received: 03.03.2025

INVESTIGATION OF PHYSICO-CHEMICAL, X-RAY AND ELECTROPHYSICAL PROPERTIES OF THE OBTAINED PHASES IN THE Ga_2Sr-SrSe SYSTEM

I.I. ALIYEV[1], N.I. YAGUBOV[2], A.N. SULTANOVA[2], A.A. HASANOV[3], A.T. MAMMADOVA[4]

[1]Institute of Catalysis and Inorganic Chemistry named after M. Nagiyev, Ministry of Science and Education of the Republic of Azerbaijan
[2]Baku State University, Baku, st. Z. Khalilov, 23.
[3]Azerbaijan State University of Oil and Industry
[4]Ganja State University

Using methods of physicochemical analysis (DTA, XRF, MSA, as well as density and microhardness measurements), the chemical interaction in the Ga_2Sr-SrSe system was studied and its T-x phase diagram was constructed. It has been established that the Ga_2Sr-SrSe system is a quasi-binary section of the Sr-Ga-Se ternary system and belongs to the eutectic type. In the Ga_2Sr-SrSe system, there are limited regions of solid solutions based on the initial components at room temperature. Microstructural analysis showed that at room temperature, solid solutions based on the Ga_2Sr compound reach 5 mol % SrSe, and based on SrSe-3.5 mol % Ga_2Sr. The composition of the eutectic formed between the Ga_2Sr and SrSe compounds is 25 mol % SrSe, at a temperature of 850°C. The lattice parameters were calculated as a result of X-ray diffraction analysis of solid solutions $(SrSe)_{1-x}(Ga_2Sr)_x$ (x=0.01; 0.02; 0.03), respectively: for the SrSe compound, a=6.243 Å (SrSe) and for alloys solid solutions, a=6.263 Å (1 % Ga_2Sr), a=6.275 Å (2 % Ga_2Sr), a=6.298 Å (3 % Ga_2Sr). The temperature dependence of electrical conductivity and thermo-EMF of solid solution alloys $(SrSe)_{1-x}(Ga_2Sr)_x$ (x=0.01; 0.02; 0.03) on composition was studied.

Keywords: system, phase, quasi-binary, eutectic, microhardness
DOI:10.70784/azip.1.2025137

INTRODUCTIONS

It is known from the literature that chalcogenides of the main elements of subgroup II and ternary phases obtained on their basis are used as energy converters [1-6]. The chemical interaction of chalcogenides of elements of the calcium subgroup with gallium chalcogenides produces compounds containing $A^{II}MeX_2$, $A^{II}Me_2X_4$, $A^{II}Me_4X_7$ (A^{II}–Ca,Sr,Ba; Me-Ga, In, X-S,Se, Te) [7-10]. Indium chalcogenides form compounds such as $InMeX_2$, $InMe_2X_4$ (Me-Ca,Sr,Ba) [11-15]. Systems based on strontium and barium chalcogenides have been little studied. Compounds like $A^{II}MeX_2$, $A^{II}Me_2X_4$ exhibit strong luminescent properties due to the action of activators [16-20].

Previously, we studied a number of internal cross sections of the Ca-Ga(In)-Se ternary system [21-24]. The Ga_2Sr-SrSe system has not been studied.

The purpose of this work is to study the nature of chemical interaction in the Ga_2Sr-SrSe system, construct its phase diagram and detect areas of solid solution.

The intermetallic compound Ga_2Sr melts with an open maximum at 1045°C and crystallizes in the hexagonal system, lattice parameter: a = 4.344; c = 4.732 Å, sp. gr. P6/mmm [25]. The SrSe compound melts congruently at 1600°C and crystallizes in the cubic syngony, lattice parameter: a = 6.243 A, sp. gr. Fm3m, density ρ = 4.50 g/cm^3 [26].

EXPERIMENTAL PART

Alloys of the Ga_2Sr-SrSe system was synthesized from Ga_2Sr and SrSe components in quartz ampoules, evacuated to a pressure of 0.133 Pa, in the temperature range 1100-1200°C. To achieve an equilibrium state, the alloys of the system were subjected to annealing at a temperature of 700°C for 240 hours. Equilibrium alloys were studied by methods of physicochemical analysis (DTA, XRD, MSA, as well as density and microhardness measurements).

Differential-thermal analysis of the samples was carried out on a Kurnakov pyrometer NTR-73. Al_2O_3 was used as a standard; the heating rate was 10°/min.

X-ray phase analysis was performed on a D2 PHASER X-ray diffractometer. A CuKα cathode and a Ni filter were used as irradiators. Microhardness was calculated using a PMT-3 metallographic microscope. Microstructure analysis was carried out using a MIM-8 microscope. The density of the samples was determined by the pycnometric method using toluene as a filler.

The electrical conductivity and thermo-EMF of the solid solution alloys $(SrSe)_{1-x}(Ga_2Sr)_x$ (x=0.01; 0.02; 0.03) were measured in weak electric and magnetic fields (E < 10 V/cm, H < 10 kG) using a UA-1-51 electrometric amplifier using the traditional direct current method [27,28].

RESULTS AND ITS DISCUSSION

Alloys of the Ga_2Sr-SrSe system have the form of a compact mass in the temperature range of 900-1000°C and are dark gray substances. When the alloys of the system are left in the open air for a long time, they absorb air moisture and undergo hydrolysis. The alloys of the system dissolve well in strong mineral acids (HNO_3, H_2SO_4).

131, H.Javid ave, AZ-1073, Baku
Institute of Physics
E-mail: jophphysics@gmail.com

Based on the results of differential thermal analysis, it was established that two endothermic effects are observed in the thermograms of alloys of the Ga_2Sr-SrSe system. Based on the results of microstructural analysis, it was found that the solubility at room temperature in the Ga_2Sr-SrSe system based on Ga_2Sr is 5 mol. % SrSe, and based on SrSe-3.5 mol % Ga_2Sr. In Fig. 1 shows the microstructures of alloys of the Ga_2Sr-SrSe system with a content of 5, 25, 60 and 97 mol % SrSe.

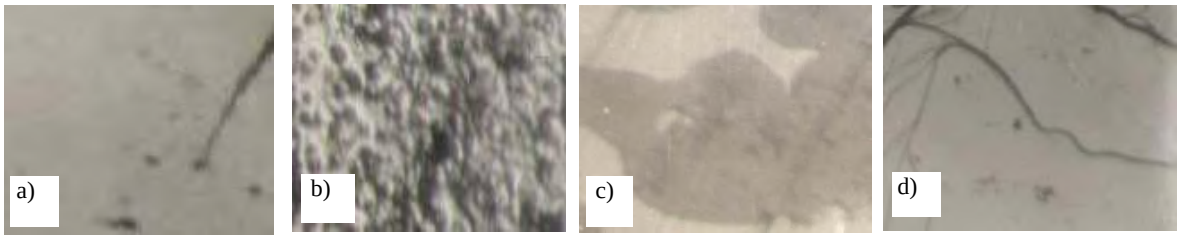

Fig. 1. Microstructures of alloys of the Ga_2Sr-SrSe system. a) -5, b) -25, c) -60, d) -96.5 mol % SrSe

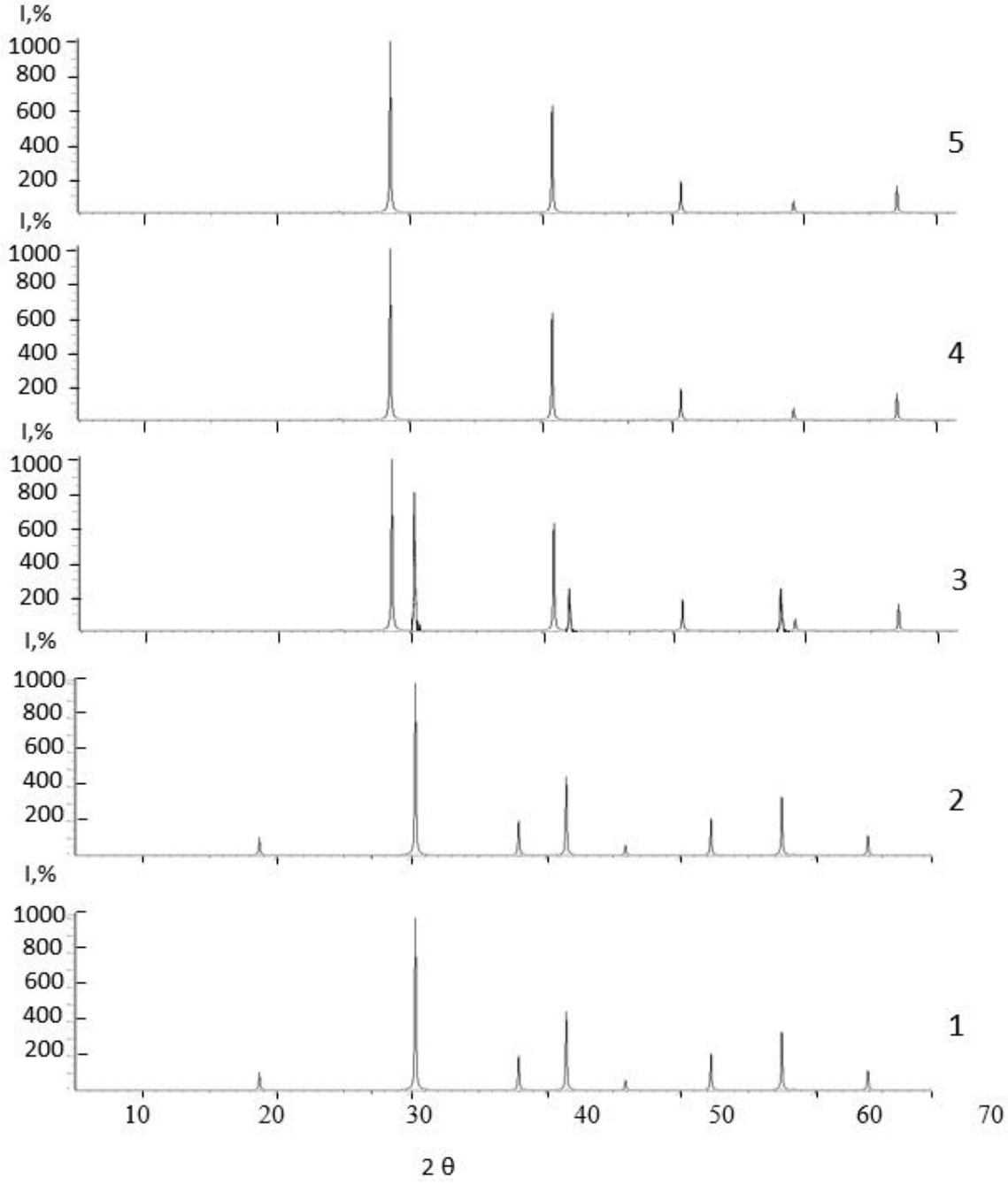

Fig. 2. X-ray diffraction patterns of alloys of the Ga_2Sr–SrSe system.
1- Ga_2Sr, 2-5, 3-60, 4-96.5; 5–100 mol % SrSe.

As can be seen from fig. 1, single-phase alloys containing 5 and 96.5 mol % SrSe are solid solution alloys based on Ga_2Sr and SrSe compounds, respectively. Alloy with SrSe content 25 mol % has a eutectic composition, and the sample with an SrSe content of 60 mol % - two-phase.

To confirm the correctness of differential thermal and microstructural analyses, X-ray phase analysis of alloys containing 5, 60 and 96.5 mol % SrSe (Fig. 2).

The diffraction maxima in the diffraction patterns of the alloys are identical to the diffraction patterns of the Ga_2Sr and SrSe compounds. That is, samples 5 and 96.5 are solid solution alloys based on Ga_2Sr and SrSe compounds, respectively. The diffraction pattern of the sample shows 60 mol % SrSe diffraction lines are a mixture of diffraction lines of the main components, i.e. it is a two-phase alloy. As a result of X-ray phase analysis, the results of DTA and MSA analyzes are confirmed.

As a result of physicochemical analysis methods, a T-x phase diagram of the Ga_2Sr–SrSe system was constructed (Fig. 3). The phase diagram of the system is quasi-binary, eutectic type. Cocrystallization of Ga_2Sr and SrSe compounds ends at the double eutectic point, composition 25 mol % SrSe, temperature 850°C.

The liquidus of the Ga_2Sr–SrSe system is limited by the monovariant equilibrium curves of an α-solid solution based on the Ga_2Sr compound and a β-solid solution based on the SrSe compound. Below the solidus line, single-phase (α) alloys crystallize in the region of 0–5 mol % SrSe, two-phase (α+β) alloys – in the range of 5–96.5 mol % SrSe, and single-phase (β) alloys crystallize in the region of 96.5-100 mol % SrSe.

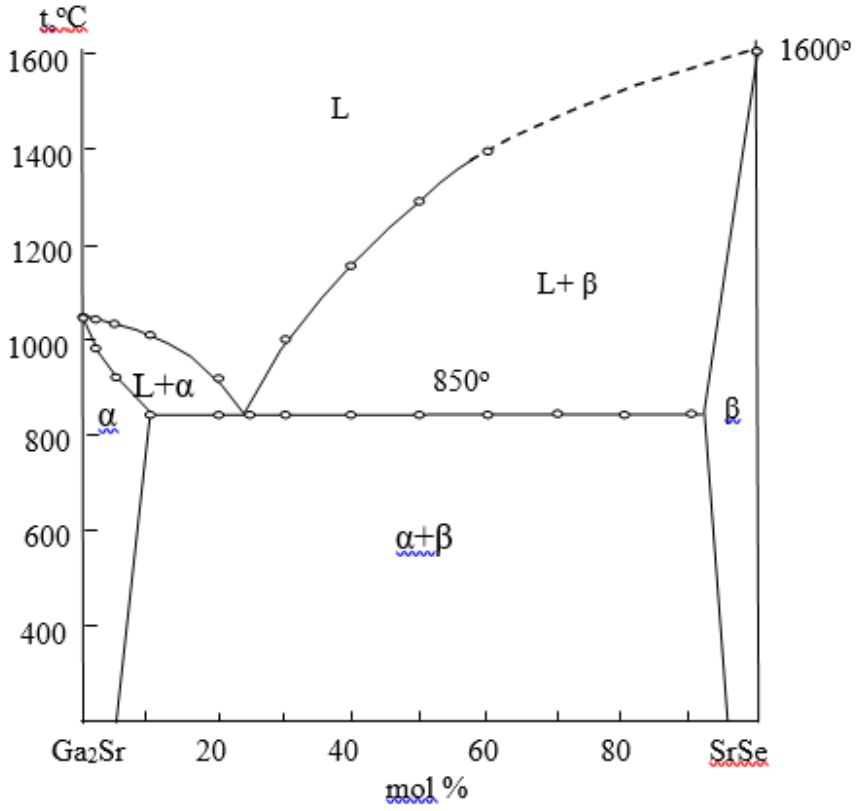

Fig. 3. T-x phase diagram of the Ga_2Sr–SrSe system.

Table 1.

Compositions of alloys of the Ga_2Sr–SrSe system, results of DTA, microhardness and density measurements

Composition, mol %		Thermal effects, °C	Density, q/cm^3	Microhardness, MPa	
Ga_2Sr	SrSe			α	β
				P=0,20 N	P=0,15 N
100	0,0	1045	4,80	2250	-
98	2,0	980,1040	4,82	2300	
95	5,0	920,1030	4,84	2300	-
90	10	850,1010	4,81	2300	-
80	20	850.925	4,75	2300	-

75	25	850	4,72	Eutec.	Eutec.
70	30	850,1000	4,71	-	-
60	40	850,1150	4,68	-	1290
50	50	850,1240	4,65	-	1290
40	60	850,1400	4,62	-	1290
30	70	850,	4,60	-	1290
20	80	850,	4,55	-	1290
10	90	850,	4,53	-	1280
0,0	100	1600	4,50	-	1250

In table table 1 shows some physicochemical properties of alloys of the Ga_2Sr–SrSe system. As a result of determining the microhardness of alloys of the Ga_2Sr–SrSe system, two different microhardness values were obtained. The microhardness value (2250-2300) MPa corresponds to the microhardness of α-solid solutions based on Ga_2Sr, and the other value (1250-1290) MPa corresponds to the microhardness of β-solid solution based on SrSe.

X-ray data of SrSe compound and alloys of the Ga_2Sr–SrSe system containing 1, 2 and 3 mol % Ga_2Sr are given in table 2.

Table 2.

X-ray data of solid solution alloys $(Ga_2Sr)_{1-x}(SrSe)_x$ (x=0.01; 0.02; 0.03)

SrSe a=6,243 Å				1 % Ga_2Sr-99 % SrSe a=6,263 Å			
I,%	$d_{eks.}$, Å	$d_{cal.}$,Å	hkl	I,%	$d_{eks.}$, Å	$d_{cal.}$,Å	hkl
100	3,1218	3,1219	200	100	3,1332	3,1326	200
50	2,2072	2,2075	220	50	2,215	2,214	220
20	2,1939	2,1937	222	20	2,2148	2,2146	222
10	1,5610	1,5608	400	10	1,5665	1,5665	400
15	1,3965	1,3960	420	15	1,4010	1,4005	420
2 % Ga_2Sr-98 % SrSe a=6,275 Å				3 % Ga_2Sr-97 % SrSe a=6,298 Å			
I,%	$d_{eks.}$, Å	$d_{cal.}$,Å	hkl	I,%	$d_{eks.}$, Å	$d_{cal.}$,Å	hkl
100	3,1391	3,1388	200	100	3,1501	3,1497	200
50	2,2192	2,2189	220	50	2,2270	2,2272	220
20	1,8123	1,8116	222	18	1,8183	1,8181	222
10	1,5691	1,5688	400	10	1,5753	1,5746	400
15	1,4038	1,4031	420	12	1,4085	1,4083	420

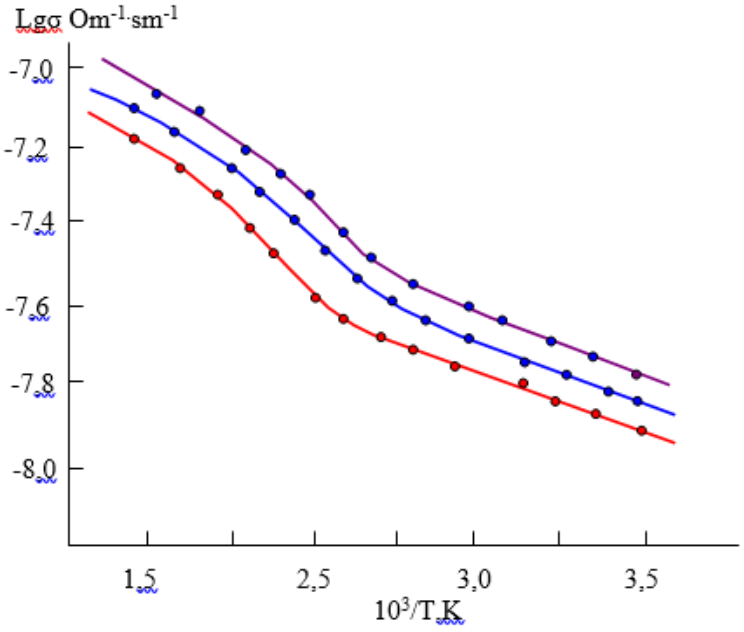

Fig. 4. The dependence of electrical conductivity of solid solution alloys $(SrSe)_{1-x}(Ga_2Sr)_x$ (x=0.01; 0.02; 0.03) on composition and temperature was studied. 1-1 mol. %, 2-2 mol. %, 3-3 mol. % Ga_2Sr.

To study the electrophysical properties of solid solution alloys $(SrSe)_{1-x}(Ga_2Sr)_x$ (x=0.01; 0.02; 0.03) containing 1; 2; 3 mol. % Ga_2Sr, they were synthesized in the temperature range of 1100-1200 °C. The samples were subjected to heat treatment at a temperature of 700°C for 100 hours for homogenization. Then the samples were shaped as a parallelepiped with dimensions of 1.2 x 1.0 x 0.8 cm^3 and physical measurements were carried out. The temperature dependence of the electrical conductivity of solid solution alloys $(SrSe)_{1-x}(Ga_2Sr)x$ (x=0.01; 0.02; 0.03) is shown in Figure 4.

With the introduction of 1; 2; 3 mol. % Ga_2Sr in the SrSe compound, the electrical conductivity, as is typical for semiconductors, increases depending on the composition and temperature.

For solid solution alloys with concentrations of 1; 2; 3 mol. % Ga_2Sr, impurity conductivity occurs in the temperature range of 300–450 K. Intrinsic conductivity begins at a temperature of 450 K. That is, electrons and holes participate in conductivity at this time.

As can be seen from Figure 4, for the samples containing 1; 2; 3 mol. % Ga_2Sr, the logarithmic values of electrical conductivity at room temperature were lgσ=-7.92 $Om^{-1}\cdot cm^{-1}$, lgσ=-7.85 $Om^{-1}\cdot cm^{-1}$ and lgσ=-7.78 $Om^{-1}\cdot cm^{-1}$, respectively. At 650 K, for the samples containing 1; 2; 3 mol. % Ga_2Sr, the logarithmic values of electrical conductivity were lgσ=-7.18 $Om^{-1}\cdot cm^{-1}$, lgσ=-7.10 $Om^{-1}\cdot cm^{-1}$ and lgσ=-7.05 $Om^{-1}\cdot cm^{-1}$, respectively.

Since the solubility limit of the Ga_2Sr compound in SrSe is not large (3.5 mol. %), it is very likely that the band structure of the obtained solid solutions is similar to the structure of SrSe. Based on this assumption, using the parameters of the zones, it is possible to calculate the electrical conductivity of the "heavy" (σ_1) and "light" (σ_2) holes and the reduced level of chemical potential ($\acute{\eta}^*$) using the formulas; $\sigma = \sigma_1 + \sigma_2$

$$\sigma_1 = 2e\left(\frac{2\pi m_0 KT}{h^2}\right)^{3/2} \cdot F_0(\eta^*)\mu_{01}\left(\frac{m_1}{m_0}\right)^{3/2}$$

$$\sigma_2 = 2e\left(\frac{2\pi m_0 KT}{h^2}\right)^{3/2} \cdot F_0(\eta^* - \Delta)\mu_{01}\left(\frac{m_2}{m_0}\right)^{3/2}$$

Where e- is the electron charge, m_0- is the mass, K -is the Boltzmann constant, h- is the Planck constant, F_0- is the Fermi integral.

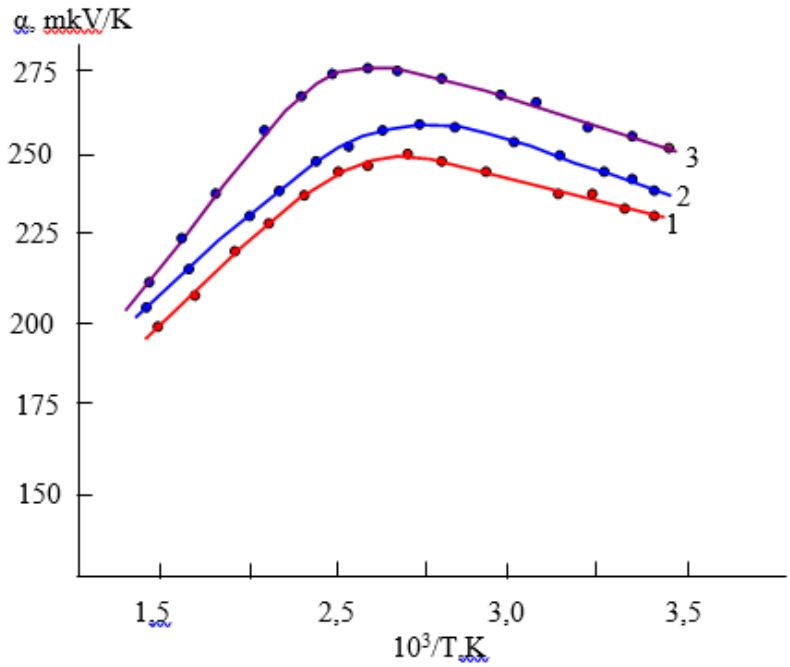

Fig. 5. Dependence of thermo-EMF of solid solution alloys $(SrSe)_{1-x}(Ga_2Sr)_x$ (x=0.01; 0.02; 0.03) on composition and temperature. 1-1 mol. %, 2-2 mol. %, 3-3 mol. % Ga_2Sr.

Fig. 5 shows the temperature dependences of thermo-EMF of solid solution alloys $(SrSe)_{1-x}(Ga_2Sr)_x$ (x=0.01; 0.02; 0.03) on composition and temperature. It follows that the thermo-EMF coefficient increases from room temperature to the transition temperature to intrinsic conductivity, and decreases in the intrinsic region. The temperature change in the thermo-EMF coefficient is in good agreement with the change in electrical conductivity of the specified solid solution alloys.

CONCLUSION

Using complex methods of physicochemical analysis, the chemical interaction in the Ga_2Sr–SrSe system was studied and its T-x phase diagram was constructed. The phase diagram of the system is quasi-binary, eutectic type. Eutectic coordinates: 25 mol % SrSe, temperature 850°C. In the Ga_2Sr–SrSe system at room temperature, solid solutions based on the Ga_2Sr compound reach 5 mol % SrSe, and based on SrSe-3.5 mol % Ga_2Sr. The lattice parameters were calculated as a result of X-ray diffraction analysis of solid solutions $(SrSe)_{1-x}(Ga_2Sr)_x$ (x=0.01; 0.02; 0.03). X-ray diffraction analysis of samples containing 1, 2 and 3 mol % Ga_2Sr, shows that these samples crystallize in the cubic syngony. The crystal lattice parameters increase accordingly in the following order: for the SrSe compound a = 6.243 Å and for solid solution alloys a = 6.263 Å (1 % Ga_2Sr) and a = 6.275 (2 % Ga_2Sr), a = 6.298 Å (3 % Ga_2Sr). The dependence of electrical conductivity and thermo-EMF of solid solution alloys $(SrSe)_{1-x}(Ga_2Sr)_x$ (x=0.01; 0.02; 0.03) on composition and temperature was studied.

[1] *Deli Jiang, Jie Li, Chaosheng Xing, Zhengyuan Zhang, Suci Meng, Min Chen.* Two-Dimensional $CaIn_2S_4$/g-C_3N_4 Heterojunction Nanocomposite with Enhanced Visible-Light Photocatalytic Activities: Interfacial Engineering and Mechanism Insight. ACS Appl. Mater. Interfaces, 2015. V. 34. № 7. P. 19234–19242. doi: 10.1021/acsami.5b05118

[2] *Jianjun Ding, Bin Hong, Zhenlin Luo, Song Sun, Jun Bao, Shen Gao.* Mesoporous Monoclinic $CaIn_2S_4$ with Surface Nanostructure: An Efficient Photocatalyst for Hydrogen Production under Visible Light. J. Phys. Chem. C, 2014. V.118 . № 48. P. 27690–2769. https://doi.org/10.1021/jp508497a

[3] *H. Hamada, I. Yoshida, Carkner Don, Wu X, M. Kutsukake, K. Oda.* Inorganic EL devices with high-performance blue phosphor and application to 34-in. flat-panel televisions. Society for Information Display. Journal. 2008. V.16. № 12. P. 1183-1188. doi:10.1889/JSID16.12.1183

[4] *D. Wauters, D. Poelman, R.L. Van Meirhaeghe, F. Cardon.* Optical characterisation of SrS : Cu and SrS : Cu,Ag EL devices. J. Lumines. 2000. V. 91. № 1–6. https://doi.org/10.3390/ma3042834

[5] *S. Tanaka, Y. Mikami, H. Deguchi, H. Kobayashi.* White-light emitting thin-film electroluminescent devices with SrS:Ce,Cl/ZnS:Mn double phosphor layers. Jpn. J. Appl. Phys. Part 2 - Lett. 1986. V.25. L225–L227. **doi** 10.1143/JJAP.25.L225

[6] *C.R. Wang, K.B. Tang, Q. Yang, C.H. An, B. Hai, G.Z. Shen, Y.T. Qian.* Blue-light emission of nanocrystalline CaS and SrS synthesized via a solvothermal route. Chem. Phys. Lett. 2002. V. 351. P. 385-390. https://doi.org/10.1016/S0009-2614(01)01413-0

[7] *Т.Н. Гулиев, П.Г. Рустамов, Н.И. Ягубов.* Взаимодействие в системе CaSe-In_2Se_3. Изв. АН СССР. Неорган. материалы. 1987. Т.23. № 9. С.1447-1450.

[8] *А.В. Кертман, О.И. Носов, О.В. Андреев.* Реакции в системе CaS-In_2S_3. Журн. неорган. химии. 2002. Т.47. № 1. С.126- 130. doi: 10.61413/Pfhg7389

[9] *Т.Н. Гулиев, Н.И. Ягубов.* Исследование взаимодействия в системе CaS-In_2S_3. Синтез и свойства неорганических соединений (Тематический сборник научных трудов) Баку. 1984. С.3-6.

[10] *О.В. Андреев, Н.Н. Паршуков.* Фазовые диаграммы системы CaS-Er_2S_3. Журн. неорган. химии. 2004. Т.49. № 11. С.1763-1766.

[11] *О.В. Андреев, О.Ю. Митрошин, Н.А. Критокин, И.А. Разумкова.* Фазовые равновесия в системе SrS-Ln_2S_3. Журн. неорган. химии. 2008. Т.53. № 3. С. 440-444.

[12] *А.В. Кертман, Н.В. Краеваб.* Фазовые равновесия в системе SrS-Ga_2S_3. Журн. неорган. химии. 2010. Т. 55. № 8. С. 1283-1286. doi: 10.61413/Pfhg7389

[13] *Chiharu Hidaka, Nobuyasu Makabe, Takeo Takizawa.* Determination of a pseudo-binary SrSe–Ga_2Se_3 phase diagram and single crystal growth of $SrGa_2Se_4$ compounds. Journal of Physics and Chemistry of Solids. 2003. V. 64, № 9–10. P. 1797-1800. https://doi.org/10.1016/S0022-3697(03)00096-9

[14] *О.В. Андреев, А.В. Кертман, В.Г. Бамбуров.* Фазовые равновесия в системах La_2S_3-SrS и Nd_2S_3-SrS. Журн. неорган. химии. 199. Т. 36. № 1. С. 253-257.

[15] *О.В. Андреев, О.Ю. Митрошин, И.А. Разумкова.* Фазовые равновесия в системах Sc_2S_3-SrS и Sc_2S_3-BaS. Журнал неорган. химии. 2008. Т. 53. № 2. С. 366-369.

[16] *W. Klee, H. Schofer.* Duratellung und krystallstructur. Von $SrIn_2Se_4$ and $CaIn_2Se_4$ Rib. Chim. miner. 1979 . V.16. P.463-466.

[17] *Б.Г. Тагиев, О.Б. Тагиев, Р.Б. Джаббаров, Н.Н. Мусаева, У.Ф. Касимов.* Фотолюминесценция в соединениях $Ca_4Ga_2S_7:Ce^{3+}$ и $Ca_4Ga_2S_7:Pr^{3+}$ Неорган. материалы. 2000. Т. 36. № 1. С. 3-6. doi: 10.61413/Pfhg7389

[18] *A.N. Georgobiani, B.G. Tagiev, S.A. Abushov, O.B. Tagiev, Zhen Xu, and Suling Zhao.* Photo– and thermoluminescence of Eu, $BaGa_2Se_4$, Eu,$BaGa_2Se_4$, Eu,Ce crystals. Inorg. mat. 2008. V. 44. № 2. P. 110 – 114. ISSN 1996-3955

[19] *H. Najafov, A. Kato, H. Toyota, K. Iwat, A. Bayramov and S. Lida.* Effekt Ce co-doping on CaGa2S4:Eu phosphor: II. Thermoluminescence. Japn. J. Appl. Phys. 2002. V. 44. P. 2058 – 2065. doi:10.1143/JJAP.41.2058

[20] *J.E. Van Haecke, P.F. Smet, D. Poelman.* The influence of source powder composition on the electroluminescence of $Ca_{1-x}Sr_xS$:Eu thin films. Spectroc. Acta Pt. B-Atom. Spectr. 2004. V. 59. P. 1759-1764.

[21] *Y.N. Yaqubov, İ.İ. Əliyev, F.İ. İsmayılov.* $CaIn_2$-CaTe sisteminin faza diaqramı. Az. Kimya jurnalı. 2014. № 1. S.70-74.

[22] *N.İ. Yaqubov, İ..İ Əliyev.* Ca_3In-CaTe sisteminin faza diaqramı BDU Xəbərləri 2014. № 3. C. 18-23.

[23] *İ.İ. Əliyev, N.İ. Yaqubov, N.A. Məmmədova.* Ca_3In-CaSe sisteminin fiziki-kimyəvi tədqiqi. Kimya Problemləri. 2013. № 4. S.432-436.

[24] *И.И. Алиев, Р.Л. Мусаева, Н.И. Ягубов, Ф.М. Садыгов, Ф.И. Исмаилов.* Характер взаимодействия в системе InSe-CaSe. Журн. неорган. химии. 2009. Т.54. № 8. С. 1398-1400.

[25] Диаграмма состояния двойных металлических систем: Справочник: В 3 т.: Т.2 / Под. Общ. ред. Н.П. Лякишева. – М.: Машиностроение. 1997-1024 с.

[26] Диаграмма состояния двойных металлических систем: Справочник: В 2 т.: Т.3 / Под. Общ. ред. Н.П.Лякишева. – М.: Машиностроение. 2000-448 с.

[27] N.B. Kolomiets. Measurement of thermoelectromotive force and resistivity in the temperature range from 20 to 1900ºC. Factory laboratory. 1962. T.28. № 2. P. 238-240.

[28] *A. Okhotin, N. Pushkarskiy, R. Borovikova, R. Smirnov.* Methods of investigation of thermoelectric properties of semiconductors. M.: Atomnzdat. 1969.175 p.

Received: 17.03.2025

ISSN 1028-8546

2025, Vol. XXXI, №1
Section: E

CONTENTS